Experimental Astrophysics: Quantum state determination and manipulation in mutual neutralisation experiments

FYP415, Bachelor Thesis

Anton Gunnarsson
Leonor Palazzo

GÖTEBORGS UNIVERSITET

gusgunanab@student.gu.se
guspalale@student.gu.se

Department of Physics, University of Gothenburg
Gothenburg, June, 2023

Abstract

Reactions and interactions between ions in plasmas are crucial phenomena that drive the evolution of matter in the universe. Specifically, mutual neutralisation (MN) is a charge transfer collision between two oppositely charged ions, which is very efficient at the low collision energies and low temperature found in the interstellar medium. The presence of HeH^+ in the early universe is thought to have significant importance in the formation of stars and was recently found in planetary nebulae, opening up new questions regarding its role. However, its presence is hard to detect by observation, and only by studying HeH^+ in collisions such as MN in a laboratory, can we gain fundamental knowledge to improve our models. Here we present a final-state-resolved MN experiment of HeH^+ with D^- performed at the world-unique facility Double ElectroStatic Ion Ring ExpEriment (DESIREE) in Stockholm, Sweden. The MN of HeH^+ and D^- resulted in the three neutral products $He(1s^2)$ + $H(n = 2)$ + $D(1s)$ corresponding to a kinetic energy release of about 1 eV. A first analysis suggests that MN leading to $He(1s^2)$ + $H(n = 1)$ + $D(1s)$ through radiative dissociation from the intermediate $HeH^*(C\ ^2\Sigma^+)$ state was also observed. We suspect this experiment to be studied again at various energies in the future, to obtain cross sections and branching ratios which can be used in models. A proof of principle MN experiment with Na^+ and Si^- was also conducted, namely the manipulation of the quantum state population in the ion beam by laser photodetachment. The effect of the selective depletion was visible though not complete, needing further investigation. This technique will allow for more detailed MN studies to be investigated at DESIREE in the future.

Contents

1 Introduction

In the early moments after the Big Bang, the Universe existed in a state of hot high density plasma gradually cooling as the Universe began to expand. Once temperatures reached around 4000 K ($z = 2500$[1] or after 100 000 years), ions that had formed during the pre-recombination period began to combine with free electrons, forming neutral atoms. Naturally, recombination first occurred for atomic ions with the highest ionization energy (IE); meaning that He^{++} and He^{+}, with IE = 54.5 eV and IE = 24.6 eV respectively, recombined and formed the first neutral atom, He. These newly formed helium atoms started to interact with preexisting protons via the direct radiative association process

$$He + H^{+} \rightarrow HeH^{+} + h\nu, \tag{1}$$

forming the very first molecule, HeH^{+} [1]. Later, another channel for producing HeH^{+} opened up via the radiative association process

$$He^{+} + H \rightarrow HeH^{+} + h\nu. \tag{2}$$

The presence and effect of HeH^{+} in space are not well known for several reasons, but the latest research suggests that it could have a more important role than previously thought, both in primordial times and today. Although speculated for a long time, the presence of HeH^{+} in planetary nebulae was finally confirmed in 2019 thanks to advances in technology [2]. The detection was made by the high altitude SOFIA telescope that looked at the NGC 7027 nebula and was able to observe the 149.1 µm rotational ground state transition for HeH^{+}, which is the prominent spectral line of HeH^{+}. The close proximity of CH spectral lines at 149.09 µm and 149.39 µm had made this measurement hard to achieve until sufficiently advanced spectroscopic equipment, as used on SOFIA, was made available. In stars, there are models predicting the presence of HeH^{+}, but any confirming observations are yet to be made. Early stars containing primordial HeH^{+} could have masses as low as 0.2 $M_{\odot}$[2] [3], with the star HE0107-5240 being a possible candidate. Stars containing larger amounts of HeH^{+} are expected to have a high number fraction of helium, very low density, and a temperature of ∼3500 K [3]. These conditions could meet not only in primordial stars but also in white dwarfs.

The presence of primordial molecules such as HeH^{+}, H_2, HD, and LiH is an important factor in the formation of the first stars. Because of their rotational de-excitations, molecules with a relatively strong dipole moment are most effective at cooling down molecular clouds, thereby initiating star formation. HeH^{+} should be regarded as a key element in star formation due to its high abundance relative to other high-dipole-moment molecules [4, 5]. Furthermore, the production of HeH^{+} might have been enhanced by about 25% through stimulated radiative association in the early universe, thus making it more abundant than previously thought [6].

A deeper understanding and modeling of the presence of HeH^{+} requires us to study the processes and impact related to its destruction in a laboratory setting. HeH^{+},

[1] z is the cosmological redshift.

[2] $M_{\odot} = 1.988\,47 \times 10^{30}$ kg, is the solar mass.

being found in plasmas, interacts with free electrons and other ions. Typically, a plasma rich of free electrons will have a high rate of cation neutralisation by recombination, dissociative recombination (DR) in the case of HeH^+. Once most electrons have reacted with the positive ions, charge transfer reactions such as mutual neutralisation (MN) between two oppositely charged ions will come into play [7]. Studies of MN are performed both in plasma measurements, obtaining reaction rates, and in ion beam experiments, determining cross sections. The latter takes advantage of the capacity of ions to be accelerated by electrostatic fields to create ion beams. At the UCLouvain, a single-pass merged beam apparatus is used to perform such cross section measurements. The location of the MN reaction can be accurately determined using this technique, thereby improving the accuracy of the kinetic energy release [8]. On the other hand, a single pass means that many quantum states of the ions are populated, leading to a "forest" of energies released, which can be challenging to sort out.

High-precision measurements of ions are made possible by storing them in cryogenic rings. Under these conditions, ions radiatively relax from their excited rovibrational states. There are today three facilities in the world that have super-cooled electrostatic ion storage rings: the Cryogenic Storage Ring CSR [9] in Germany, the RIKEN Cryogenic Electrostatic (RICE) ring in Japan [10], and the Double ElectroStatic Ion Ring ExpEriment (DESIREE) in Stockholm, Sweden [11, 12]. Only DESIREE has the capability of performing MN experiments thanks to its double ring with a merging region. Negative and positive ions are injected and circulated in each ring simultaneously. Since MN reactions only take place at very low collision energies, the velocities of the beams are adjusted in the merging region by applying an electric voltage, effectively reducing the center-of-mass collision energy to a few meV. The reaction rate of MN is highly dependent on the states occupied by the interacting ions. With internally relaxed ion beams, the determination of the quantum states of the neutral products is then possible. This makes DESIREE a world-unique facility exceptionally suitable for studies of MN. Furthermore, the capability to store ions for extended durations also allows the manipulation of selected quantum states. Developing such techniques opens up new opportunities to test theoretical models and to better replicate astrophysical environments in laboratory settings.

Astrophysics has, for the most part, been an observational science. But facilities such as DESIREE are now allowing so-called experimental astrophysics to complement knowledge acquired in the past. For instance, stellar atmosphere models, such as non-local thermodynamical equilibrium (non-LTE) methods, take into account the rate coefficients of collisions [8]. It is therefore highly desirable for such experimental measurements to be made in order to complement and better refine our theories and models. With HeH^+ being present in both stellar and planetary atmospheres, it is therefore of interest to study these processes in laboratory settings.

Fortunately, the dissociative recombination (DR) of HeH^+ has already been studied extensively. MN, on the other hand, needs more investigations. Results from a DR experiment indicate that the quantum states of the products of DR at 0 eV collision energy predominantly produces He in its ground state and H in $n = 2$

excited state [13].

The aim of our experiment is to study the MN of HeH^+ with H^- and to determine the quantum states of the neutral products. The hydrogen anion was a natural choice since it populates most plasmas where HeH^+ is found. Due to the mass per energy ratio limits imposed by the experimental setup, the actual ions studied were HeH^+ and D^-. Because of the particular characteristics of HeH^+, MN could theoretically occur both by electron transfer, which is the common process in MN or by proton transfer. Both processes were analyzed.

With the capabilities of DESIREE, developing and refining new high-precision experimental techniques are crucial. This is why a second experiment involving the manipulation of quantum states of the injected negative ion was performed. Suitable candidates for this experiment were Si^- and Na^+, because of their mass ratio and the appropriate energies of the excited metastable state of Si^-. This is a proof of principle experiment which hopefully will enable more detailed studies of MN reactions of astrophysical relevance in the future.

2 Theory

The study of ions is crucial in plasma physics and in fundamental atomic and molecular physics. The primary interests of these studies are to measure fundamental properties such as electron affinity (EA) and lifetimes of metastable states as well as to investigate charge transfer processes. These include electron-ion recombination [14], ion-neutral electron transfer, electron attachment to neutrals [15] and ion-ion recombination (radiative, by triple collisions, or by mutual neutralisation) [14]. This report will present experiments involving mutual neutralisation.

2.1 Mutual neutralisation - MN

Mutual neutralisation is a process that occurs between two oppositely charged atomic or molecular ions where both ions are neutralised via a charge exchange, usually an electron:

$$\mathrm{A}^+ + \mathrm{B}^- \rightarrow \mathrm{A}^* + \mathrm{B}^* + E_K. \tag{3}$$

The probability of such events is higher than for electron-ion recombination since the relative velocities of the reactants are lower between ions [14]. For the excess electron to be transferred from the anion to the cation, the ionization energy of the cation needs to be higher than the electron affinity of the anion. Any excess energy gained by the cation is subsequently converted into excitation of the neutral product [15]. This reaction is therefore exothermic meaning that energy is released in the form of kinetic energy and excitation energy of one or both of the neutral products. The kinetic energy released is determined by

$$E_K = \underbrace{\left[IE(A^0) + E_{lvl}(A^+) - E_{lvl}(A^0)\right]}_{\text{Binding energy of anion, } E_b(A^+)} - \underbrace{\left[EA(B^0) + E_{lvl}(B^0) - E_{lvl}(B^-)\right]}_{\text{Binding energy of cation, } E_b(B^{-*})}, \tag{4}$$

where $IE(A^0)$ is the ionization energy, EA is the electron affinity, and E_{lvl} is the level energy. Therefore, by measuring the released kinetic energy during MN, valuable information can be obtained regarding the initial quantum states of the ions and the quantum states of the resulting neutral products.

When analyzed theoretically, mutual neutralisation events are treated as crossings between the potential energy curves of ionic and covalent states in the interacting ions [7]. As presented by the Landau-Zener model, this crossing also determines the critical interatomic distance, R_c, at which the MN takes place. Since this distance is relatively large, any multipolar interaction is negligible. The energy difference between the covalent and ionic state, when the interatomic distance is infinite, corresponds to the kinetic energy release, E_K. These characteristics, coupled with the Coulomb attraction between the ions, make MN a highly efficient process.

2.2 Manipulation of quantum levels with lasers

Negative ions do not form as easily as positive ions since they need to have an electron configuration that can accommodate an extra electron. Even less common

are negative ions that have a bound electronic excited state. Depending on the lifetimes of these excited states, it can be tricky to isolate the ground state and perform experiments only regarding the ions in their ground state. Ions in long-lived metastable states can therefore resist thermal relaxation during experiments. However, there are alternative methods for manipulating the populated states in the ion beams, one of which is using a laser. The energy of a laser can be adjusted to exceed the binding energy of the outermost excited electron in undesired states, without reaching the energy of the electron affinity. This results in the targeted ions being converted to neutrals through photodetachment. These neutrals are no longer affected by the electromagnetic components of the storage rings and continue in a straight path. This effectively depletes the ion beam of the selected excited states.

2.3 Channels

During a reaction such as MN, the reactants' energy potentials interact in such a way that several quantum states might be populated in the products. This can in turn lead to a sequential reaction. These different scenarios are called channels, and, depending on the cross section of each channel, branching ratios can be estimated.

Relying on previous studies, both experimental and theoretical, several channels were theorized for both experiments presented here. In all cases, the anion was expected to become a neutral atom in its ground state after the MN.

2.3.1 Experiment 1: HeH^+ / D^-

In the HeH^+ and D^- MN, there are four theorized possible channels with two or three products that can arise from electron transfer, as shown in Fig. 1. These are

$$\mathrm{HeH^+ + D^-} \rightarrow \begin{cases} \mathrm{HeH^* + D} \quad \rightarrow \quad \mathrm{He + H}(n=2) + \mathrm{D} & 0.8020\ \mathrm{eV} \\ \mathrm{HeH^* + D} & 1\text{–}3\ \mathrm{eV} \\ \mathrm{HeH^* + D} \quad \rightarrow \quad \mathrm{He} + h\nu + \mathrm{H}(n=1) + \mathrm{D} & 1\text{–}10\ \mathrm{eV} \\ \mathrm{He + H}(n=1) + \mathrm{D} & 11.0009\ \mathrm{eV}. \end{cases}$$

The neutral molecule HeH is dissociative in its ground state. If the MN reaction leads to neutral products in their ground states, this channel would therefore release 11.0009 eV and three neutral products. There are also several metastable excited states, HeH^*, which can lead to dissociation with $H(n = 2)$, or, after deexcitation through photon emission, $H(n = 1)$. If the metastable state lives long enough, two products are expected to be detected with $E_K = 1\text{–}3$ eV.

A neutralisation reaction can also occur via proton transfer, leading to the creation of a hydrogen molecule (HD) and a helium atom as neutral products, creating a $E_K = 14\text{–}16$ eV channel. The hydrogen molecule can also dissociate through two different channels with $H(n = 1)$ or $H(n = 2)$. Visualized in Fig. 2, the channels

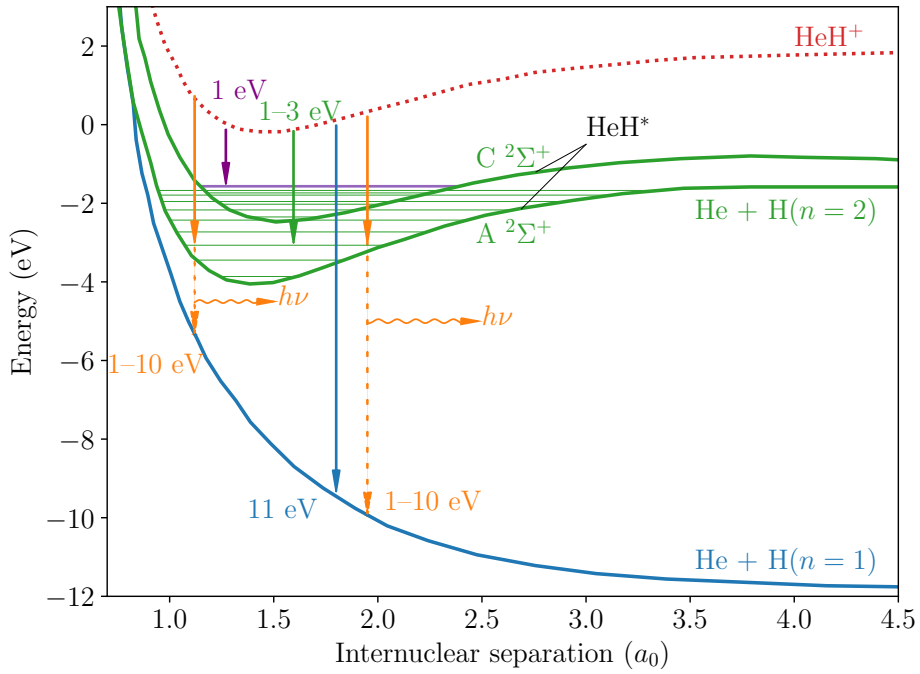

Figure 1 – Potential energy as a function of internuclear separation for four channels resulting from electron transfer between HeH^+ and D^-. The channels are represented by color-coded arrows. After accounting for the electron affinity of D^-, the length of the arrows represents the kinetic energy release for each channel.

created by proton transfer are therefore

$$\mathrm{HeH^+ + D^-} \rightarrow \begin{cases} \mathrm{He + HD} & & & 14\text{–}16\,\mathrm{eV} \\ \mathrm{He + HD^{**}} & \rightarrow & \mathrm{He + H}(n=1) + \mathrm{D} & 11.0009\,\mathrm{eV} \\ \mathrm{He + HD^{*}} & \rightarrow & \mathrm{He + HD^{**}} + h\nu & \\ & \rightarrow & \mathrm{He + H}(n=1) + \mathrm{D} & 5\text{–}9\,\mathrm{eV} \\ \mathrm{He + HD^{*}} & \rightarrow & \mathrm{He + H}(n=2) + \mathrm{D} & 0.8020\,\mathrm{eV}. \end{cases}$$

Presented in table 1 are the values used for the estimated kinetic energies for both the electron and proton transfer channels.

Table 1 – Proton affinity, PA, for HeH^+ [16], dissociation energy, DE, for HD [17], ionization energy, IE, for H and electron affinity, EA, for D both from the NIST database.

PA of HeH^+ (eV)	DE of HD (eV)	IE of H (eV)	EA of D (eV)
1.843	4.5136	13.59844	0.75458

2.3.2 Experiment 2: Na^+ / Si^-

The negative silicon ion Si^- has a $^4S^o$ ground state, a metastable $^2D^o$ excited state at 0.867 eV, and a $^2P^o$ excited state at 1.361 eV above the ground state [18]. Only the

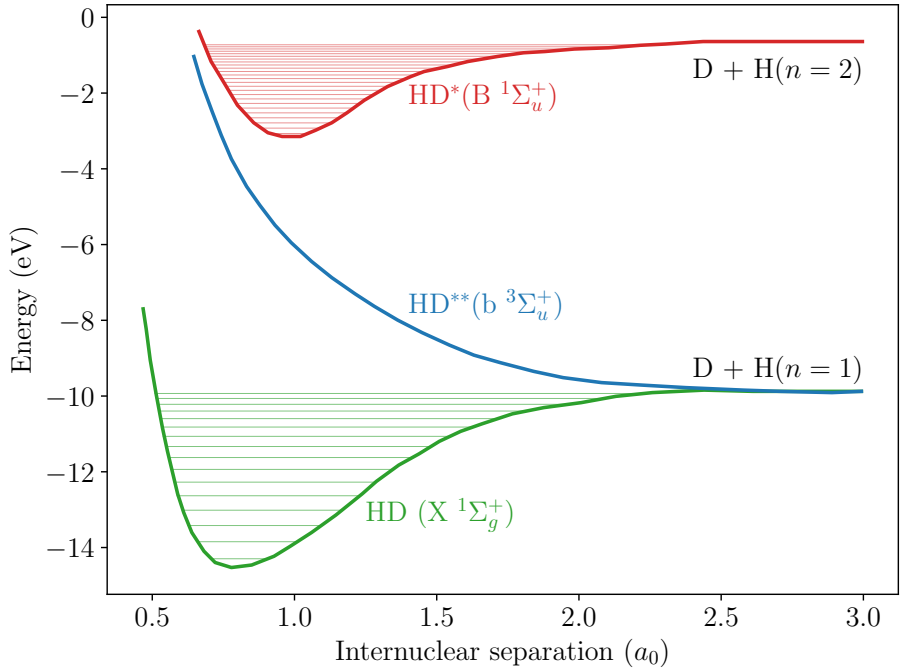

Figure 2 – Potential energy curves corresponding to the three possible channels for proton transfer from HeH^+ to D^-.

ground state and the $^2D^o$ state were expected to be populated during the experiment because the $^2P^o$ state is barely bound with only ∼0.035 eV. Depending on the state of Si^- before the MN reaction, four different channels were predicted with ACAM calculations performed by the theorist, Dr. A. Dochain [7]. The simulated spectrum in Fig. 3 shows the resulting predicted channels. The ground state of Si^- ($^4S^o$) is expected to populate the Na ($3p\ ^2P^o$) state, with a kinetic energy release of 1.7 eV. Similarly, Fig. 4 shows that transitions from the excited $^2D^o$ state to the Na $3d\ ^2D$, $4p\ ^2P^o$ and $5s\ ^2S$ states are expected. The corresponding energy levels are shown in Fig. 5, illustrated by blue and red dots.

The kinetic energy release for all possible channels are

$$\mathrm{Na}^+(2p^6\ ^1S) + \mathrm{Si}^-(3p^3\ ^4S^o) \quad \rightarrow \quad \begin{cases} \mathrm{Na}(2p^6 3s\ ^2S) + \mathrm{Si}(3p^2\ ^3P) & 3.7541\,\mathrm{eV} \\ \mathbf{Na(2p^6 3p\ ^2P^o) + Si(3p^2\ ^3P)} & \mathbf{1.6504\,eV} \\ \mathrm{Na}(2p^6 4s\ ^2S) + \mathrm{Si}(3p^2\ ^3P) & 0.5627\,\mathrm{eV} \end{cases}$$

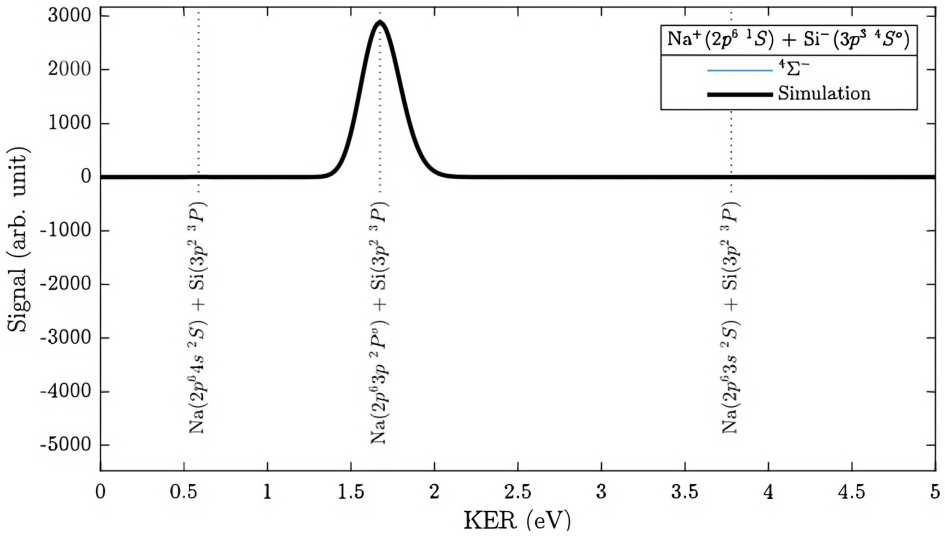

Figure 3 – Simulation of the kinetic energy release (KER) for transitions during MN of Na^+ $(2\mathrm{p}^6\ {}^1S) + \mathrm{Si}^-$ $(3p^3\ {}^4S^o)$.

$$\mathrm{Na}^+(2p^6\ {}^1S) + \mathrm{Si}^-(3p^3\ {}^2D^o) \quad \rightarrow \quad \begin{cases} \mathrm{Na}(2\mathrm{p}^6 3p\ {}^2P^o) + \mathrm{Si}(3p^2\ {}^1D) & 1.7314\,\mathrm{eV} \\ \mathrm{Na}(2\mathrm{p}^6 4s\ {}^2S) + \mathrm{Si}(3p^2\ {}^1D) & 0.6437\,\mathrm{eV} \\ \mathbf{Na(2p^6 3d\ {}^2D) + Si(3p^2\ {}^3P)} & \mathbf{0.9991\,eV} \\ \mathbf{Na(2p^6 4p\ {}^2P^o) + Si(3p^2\ {}^3P)} & \mathbf{0.8630\,eV} \\ \mathbf{Na(2p^6 5s\ {}^2S) + Si(3p^2\ {}^3P)} & \mathbf{0.4997\,eV} \\ \mathrm{Na}(2\mathrm{p}^6 4d\ {}^2D) + \mathrm{Si}(3p^2\ {}^3P) & 0.3326\,\mathrm{eV} \\ \mathrm{Na}(2\mathrm{p}^6 4f\ {}^2F^o) + \mathrm{Si}(3p^2\ {}^3P) & 0.3279\,\mathrm{eV} \\ \mathrm{Na}(2\mathrm{p}^6 5p\ {}^2P^o) + \mathrm{Si}(3p^2\ {}^3P) & 0.2714\,\mathrm{eV}, \end{cases}$$

where the four channels with the largest amplitudes are shown in bold font.

The values necessary for these evaluations were taken from the NIST database, where some are shown in table 2.

Table 2 – Ionization energy (IE) and electron affinity (EA) from the NIST database used for the estimates of E_K.

IE of Na (eV)	EA of Si (eV)
5.13907696	1.389517

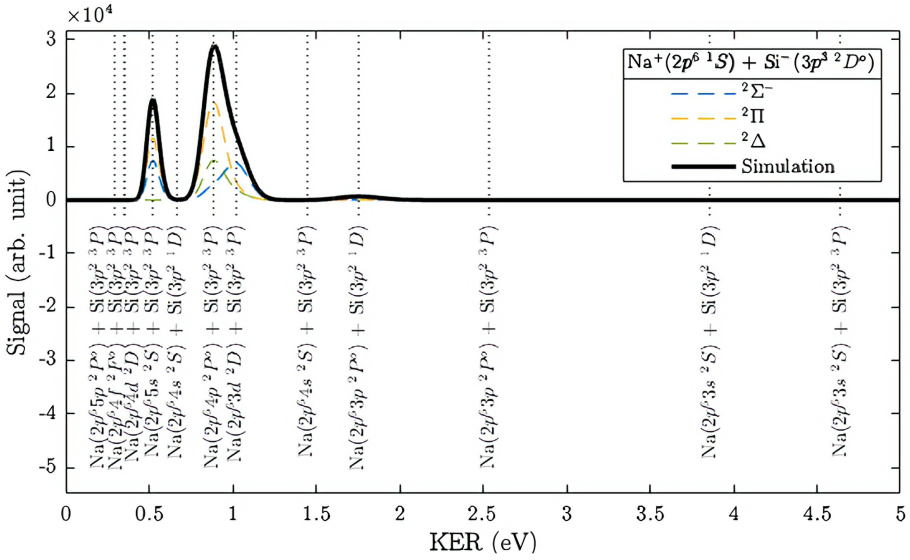

Figure 4 – Simulation of the kinetic energy release (KER) for transitions during MN of Na^+ $(2p^6\ ^1S)$ + Si^- $(3p^3\ ^2D^o)$.

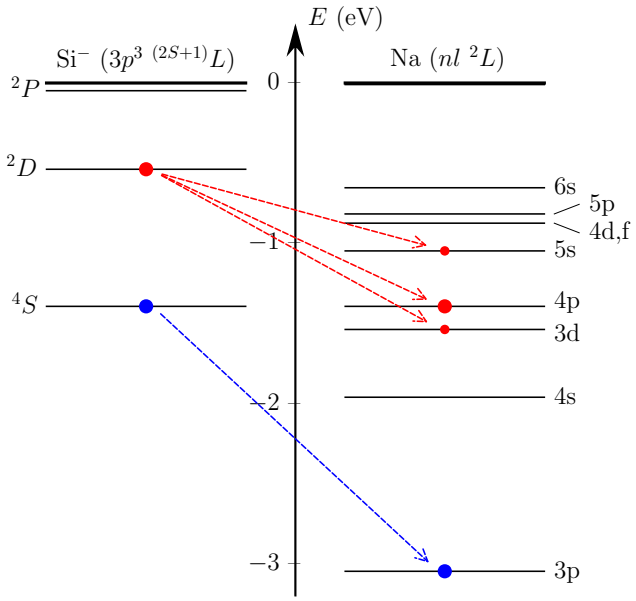

Figure 5 – Quantum states of Si^- and Na with expected channels color-coded in red and blue.

3 Experimental setup: DESIREE

The Double ElectroStatic Ion Ring ExpEriment, or DESIREE, is a facility located in Stockholm which was developed for studies of ions. The facility houses a double ion-beam storage ring set inside a cryogenically cooled (13 K), low pressure (10^{-14} mbar) environment [19]. This creates the proper conditions allowing long storage times of atomic and molecular ions prior to their study. A common merged section between the rings facilitates collision experiments between negative and positive ions with center of mass energies down to ∼10 meV. Typical studies that are performed using this unique feature are MN experiments [20, 21]. Long-time storage with cryogenic temperatures also makes DESIREE suitable for more fundamental studies of ionic properties, such as electron affinity and lifetimes of ionic metastable states. In fact, researchers in 2015, were able to measure the radiative lifetime of spontaneous transitions in the upper levels of sulfur anions to 503 ± 54 s, making it the longest lifetime ever to be measured in a negative ion [22].

3.1 Cryogenic chamber

The storage rings are situated inside a double-layered vacuum chamber with the outer chamber made out of steel and the inner chamber made out of an aluminum alloy. Situated in between the sections is a copper screen and a super-insulating material that separates the copper from the outer steel casing. Cryogenic coolers are coupled to the thermally conductive copper screen which is able to cool the inner chamber to a temperature of ∼13 K.

With the use of vacuum pumps, the outer casing is brought to a pressure of $\sim 10^{-5}$ mbar. Pressurizing the outer steel chamber serves to insulate the innermost chamber as well as to shield it against atmospheric pressure. The inner chamber, in which the ions are stored, is further brought down to a pressure around 10^{-14} mbar. The low-pressure setting allows for investigations of loosely bound systems such as negative ions, as destructive residual gas collisions are minimized. This also assists in reducing background data.

3.2 Storage rings

The ion-beam storage rings are situated inside a cryogenic chamber and a schematic view of the ion-optical ensemble can be seen in Fig. 6. The ion-optical elements are mounted onto a shared base plate where they are arranged to produce two storage rings with a common merging region (MR) in the middle. The ring on the bottom of Fig. 6 is referred to as the symmetric ring (S-Ring), and the ring on top as the asymmetric ring (A-Ring). Two injection lines, one for each ring, are positioned on the left side of the figure. Inside the rings, the ion beams are guided by electrostatic deflecting elements. Each ring is equipped with two 160° deflectors (DE-160), four 10° deflectors (DE-10), and two shared DE-10 elements at each end of the merging region. Unique to the asymmetric ring (A-Ring), and giving it its name, is an additional pair of deflecting elements (DE) placed before and after the shared deflectors on each side of the MR. These additional deflectors

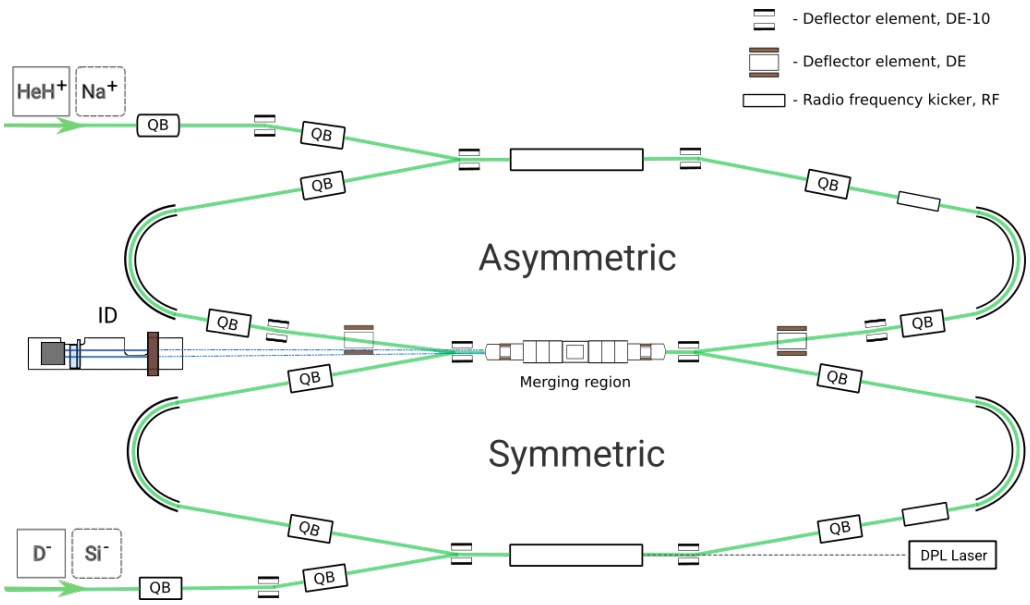

Figure 6 – Schematic view of the double storage-ring assembly.

allow for heavier ions to be stored in the A-Ring while still achieving a co-linear beam in the MR. Focusing of the beams is performed by four quadrupole doublets (QD) in each of the rings.

3.3 Ion sources

The facility is equipped with a number of ion sources but only the ones relevant for this experiment will be presented here. Most production of negative ions is done using a cesium sputter ion source (SNICS) [23]. Here, cesium is vaporized and flows into a region between a high-temperature ionizing surface and a low-temperature cathode. Subsequently, Cs^+ ions are formed in a surface ionization process on the hot ionizer surface, and some condense onto the surface of the cathode. A bias voltage applied to the cathode then accelerates the Cs^+ ions towards the cesium surface of the cathode. Upon impact, the ionized cesium sputters atoms or small molecules from the selected cathode material. The sputtered particles exchange electrons with cesium atoms while passing through the condensed layer on the cathode surface. Once produced, the negative ions are accelerated away from the cathode and focused into an ion beam.

There are a number of positive ion sources, most of which involve electron ionization processes where electrons collide with atoms or molecules of the chosen material. The first positive ion source is an Electron-cyclotron-resonance (ECR) ion source. The ECR holds plasma inside a volume that is subjected to a magnetic field. Electrons contained in the volume are then exposed to alternating electric fields that coincide with the resonant frequencies of the electrons. The alternating electric field, in combination with the magnetic field, sets electrons into a helix-shaped orbit while gaining kinetic energy. The neutral parent of the desired ion is subsequently injected as a gas into the electron-filled volume where it gets ionized through collisions with electrons.

The second positive ion source is a Nielsen-type hot filament penning magnetron ion source (NIS) [24]. The NIS contains a cylindrical filament cathode (Tantalum or Tungsten) which is enclosed by a Molybdenum anode. A low voltage high current source is used to electrically heat up the filament cathode to 2400 °C. Subsequent to being heated, the filament emits free electrons which are accelerated towards the anode encasing. Solenoids positioned outside the casing produce magnetic fields perpendicular to the electric field lines inside the chamber. The combined fields exert a Lorentz force on the electron which is set in a circular motion along the axis of the filament. As in the ECR, the neutral gas of the desired ion is then injected into the chamber and gets ionized via electron collisions. The positive ions are extracted with an acceleration voltage.

The production of ions often results in a wide distribution of populated states. Moreover, impurities and trace amounts of residual gas inside the ion sources can result in the production of several different ion species. The high energy used in the production also enables a variety of isotopes to be generated. The ions of interest are extracted by mass-to-charge ratio with the use of a mass-spectrometer. Two independent 90° deflectors are used to direct both beams toward the cryogenic chamber. During injection, a 10° deflector element (DE-10) is switched on to deflect a bunch in a ring and is rapidly switched off, keeping the bunch in the ring.

3.4 Detector and merging region

Investigations of MN events involving neutral products rely on the ability to detect the displacements of the separated products from the trajectory of the beam, which, in turn, relates to their kinetic energy. In addition, temporal measurements must be made in order to determine coincidences and to determine the separation of the particles. The detection system at DESIREE consists of three stacked micro-channel plates (MCP) coupled to a phosphor screen[3]. Incident-neutral particles strike the inner wall of the outermost MCP, freeing a few electrons. These free electrons are accelerated in an electric field, thus striking the inner wall again and releasing two or more new electrons. Each collision multiplies the number of electrons and stacking several MCPs can generate a shower of 10^8 electrons from a single neutral particle input. The shower of accelerated electrons hits a phosphorous screen which subsequently emits light through de-excitation, effectively converting the electrons to photons. The photons are detected by an event-driven TIMEPIX 3 camera (TPX3) at the end of the detection system. The TPX3 is equipped with a 256×256 pixel matrix, where each sensor pixel is capable of recording the arrival time, response duration, and coordinates of detections with a time resolution of 1.56 ns.

The merging region, including the biased region, is essential to conduct merged-beam experiments at DESIREE. It consists of seven independently controlled drift tubes that facilitate the merger of the two ion beams. Voltage is applied to the drift tubes and accelerates the incident ion beams in opposing directions. This allows control over the center-of-mass collision energy of the experiment, which can be

[3]P24 (ZnO) phosphor screen

calculated as

$$E_{CM} = \frac{m_1\, m_2}{m_1 + m_2} \left[\sqrt{\frac{E_2}{m_2}} - \sqrt{\frac{E_1}{m_1}} \right]^2 . \tag{5}$$

Each ion beam has its own velocity which depends on the beam energy as

$$v = \sqrt{\frac{2E}{m}}. \tag{6}$$

These velocities increase or decrease under the effect of the voltage U applied in the biased region. They are therefore

$$v_{\pm} = \sqrt{\frac{2E_1 \mp eU}{m}}, \tag{7}$$

with v_+ corresponding to the cation velocity and v_- to the anion. The appropriate voltage U_0 to be applied for both beams to reach the same velocity is

$$U_0 = \frac{E_1 m_2 - E_2 m_1}{e(m_1 + m_2)}. \tag{8}$$

With typical energies and masses used at DESIREE, the center-of-mass collision energy outside the biased region reaches 10–20 eV and is too high for MN to take place. But, the transition between the two sections of the merging region is not sharp, and the fringe fields just outside the biased region give rise to some MN events with higher collision energy. It is, therefore, necessary to filter out collisions occurring at higher E_{CM} in the data analysis in order to improve resolution.

Studies of MN that aim at determining cross sections need to perform MN experiments at different collision energies. This is why being able to fine-tune the applied voltage is key to these studies.

With seven independent sections, this setup is flexible and can answer different needs. Several tubes can be used together for low energy beams or low cross section experiments. A stronger beam or higher cross section reaction would require a drift tube further back to be used if the products get a low fraction of kinetic energy. Conversely, if the products gain a high fraction of kinetic energy, then a drift tube closer to the detector would be used [19].

4 Data processing

4.1 Data filtering

Data processing of ion collisions involves extracting a small set of relevant data points from a large data set. Particles from collisions were detected on a phosphor screen. A camera took images of these detections, each of which was stored as a row in our data set. Each row contained information on the pixel coordinates of the detection, the time over threshold (intensity), the time after injection, and the size (number of pixels) on the camera sensor. Noise filtration was directly applied to the data where a minimum intensity and pixel area was chosen.

The first step of the data processing requires mapping back the coordinates of the camera hits in pixels to the reference frame of the phosphor screen with the origin at its center.

A single collision produces neutral particles that arrive in a determined time interval at the detector. Knowing the distance L between the biased region and the detector, the maximum kinetic energy release $E_{k_{\max}}$, as well as the speed v and total mass M of the particles, the coincidence time is estimated as

$$t_{\text{coinc}} = \frac{L}{v^2}\sqrt{\frac{2\,E_{k_{\max}}}{M}}. \tag{9}$$

From this estimate, a coincidence requirement was applied to detections that are made in succession. The typical coincidence time of MN events at DESIREE is a few hundred nanoseconds.

As presented in Sec. 3.4, the fringe field effects from the ends of the biased region give rise to a tail effect on E_K. Thus, events occurring at the ends of the biased region gain excess energy and need to be filtered out. We define θ as the angle between the beam axis and the vector between both particles. This angle should be evenly distributed. But events from the fringe fields have higher energies and therefore lie closer to the beam. For this reason, we filter out events where $\cos\theta$ is close to 1.

These early filtering procedures heavily reduce the size of the data set and the next step involves reconstructing the particle break-up in order to identify the masses of the detected particles. The derivations for the two and three products E_K are presented in detail in [15].

4.2 E_K and r for two products

From the conservation of momentum, one can show that the distance between the two products r is proportional to the square root of the energy E, $r \propto \sqrt{E}$. This distance r can be directly calculated from the data collected during the experiment through

$$r = \sqrt{r_{||}^2 + (v\Delta t)^2} \approx \sqrt{\frac{2E}{\mu}}\frac{L}{v}, \tag{10}$$

where $r_{||}$ is the distance measured on the detector, v is the average velocity of the two beams, Δt is the time difference between the product detections, μ is the reduced mass and L is the distance from the MN event to the detector.

Several approximations are made to obtain this statement. For instance, the distance between the products on the detector $r_{||}$ is approximated to the 3-D distance r, and the length traveled by the products is not exactly known but is estimated to be in the middle of the biased region. These uncertainties need to be adjusted for by simulations.

4.3 E_K and TD for three products

From the conservation of momentum, the center of mass of the particle break-up remains constant in the xy-plane, orthogonal to the direction of flight. The center of mass in the xy-plane is calculated using the expression

$$R_{cm} = \frac{1}{\sum_{i=3}^{3} m_i} \left(\sum_{i=1}^{3} m_i x_i, \sum_{i=1}^{3} m_i y_i \right), \tag{11}$$

where x_i and y_i are the coordinates from the center of the detector in both directions. With the knowledge of possible collision products, the unknown detected particles are assigned masses at random. Once every possible center of mass has been calculated, the masses are assigned according to the combination that yields a center of mass closest to the center of the overlapping ion beams. The assignment of masses and selection of the center of mass is illustrated in Fig. 7, where only three out of six combinations are shown. In the event that no combination of masses produces a center of mass within a reasonable distance from the beam overlap, the sequence of detections is rejected. Prior to determining the kinetic energy released during the particle break-ups, the particle separation along the line of flight needs to be determined for each particle. First, the mean time of arrival is determined according to

$$t_m = \frac{m_1\, t_1 + m_2\, t_2 + m_3\, t_3}{M}, \tag{12}$$

where $t_{1,2,3}$ are the arrival times for each particle and M is the total mass. Next, the three-dimensional spatial separation of each product from the center of mass is calculated:

$$r_i = \sqrt{(x_i - x_{cm})^2 + (y_i - y_{cm})^2 + v^2 (t_i - t_m)^2}. \tag{13}$$

We can now define the total displacement, TD, which represents how far apart in 3D the three particles are as the center of mass hits the detector. With the flight distance L and the velocity of the center of mass v, we obtain

$$TD \equiv \sqrt{\frac{1}{M} \sum_{i=1}^{3} m_i {r_i}^2} \approx \sqrt{\frac{2E_K}{M}} \frac{L}{v}. \tag{14}$$

From equation (14), an expression for the total kinetic energy release is given by

$$E_k \approx \frac{M}{2} \left(\frac{v\, TD}{L} \right)^2, \tag{15}$$

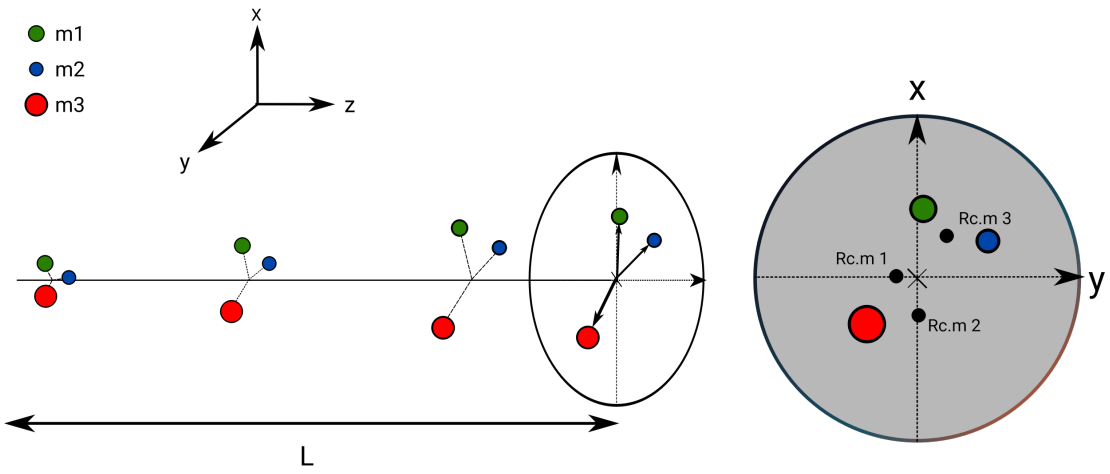

Figure 7 – Schematic of the break-up dynamics for three products with calculated positions of the center of mass for three combinations of masses.

and the energy of each particle is then given by

$$E_i = \frac{m_i v^2}{2L^2}\left(x_i^2 + y_i^2 + v^2(t_m - t_i)^2\right). \tag{16}$$

4.4 Dalitz plot

A Dalitz plot is a graphical representation of the phase space of three-body decays. Although initially used to study the decay of spinless sub-atomic particles [25], the Dalitz plot also serves as a powerful tool in investigations of non-relativistic break-ups of larger particles. An illustration of the plot is shown in Fig. 8 where the color-coded axes indicate the fraction of the energy release obtained by each product after a break-up. In the case of a break-up with three products of equal masses, each axis is orthogonal to one side of an equilateral triangle, and each vertex represents a 100% transfer of energy into one of the products. Any energetically allowed break-up is therefore constrained to lie within the triangle. Furthermore, the conservation of energy combined with the conservation of momentum constrain all possible break-ups to lie within the circle. Any point on the Dalitz plot represents the energy-sharing configuration of an event. This is illustrated with two points in Fig. 8 where the energy configuration of the break-up changes for different positions on the graph. Visualizing all measured events in this way gives insight into the distribution of kinetic transfer configurations among the products of each break-up. The density of points in any region of the plot reveals the frequency at which that specific energy distribution occurs.

In the case of three products with different masses, either the triangle or the circle will be affected. If one chooses to constrain the events to a circle, the size of the triangle sides will vary and no longer be equilateral. For a circular Dalitz plot, the

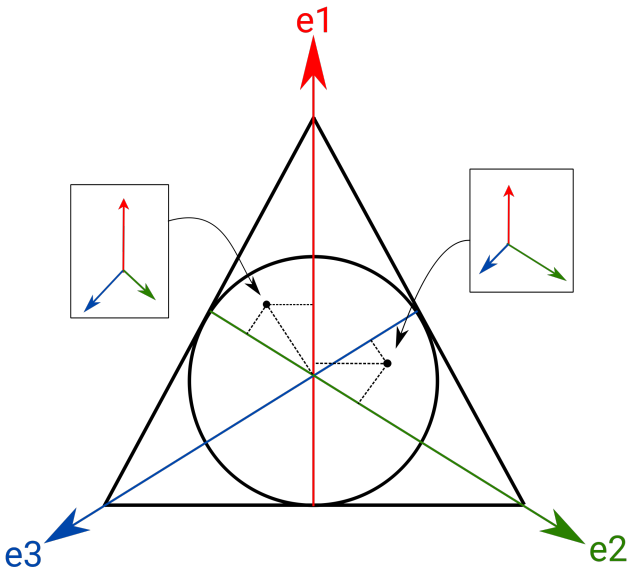

Figure 8 – Construction of a Dalitz plot in a triangular coordinate system with axes e1, e2, e3 that indicate the fraction of energy released with each product. Two example points are shown along with visual displays of their energy distribution, where the magnitude of the color-coded vectors represent the amount of kinetic energy released to the products.

coordinates (η_1, η_2) are determined by:

$$\eta_1 = a(\epsilon_1 - \epsilon_2) - b(2\epsilon_3 - 1) \qquad \eta_2 = 2\epsilon_3 - 1 \tag{17}$$

where

$$a = \frac{(M_{tot} - m_1)(M_{tot} - m_2)(M_{tot} - m_3)}{\sqrt{m_1 m_2 m_3 M_{tot}}(M_{tot} + m_3)} \qquad b = \sqrt{\frac{M_{tot} m_3}{m_1 m_2}} \frac{m_1 - m_2}{M_{tot} + m_3} \tag{18}$$

$$\epsilon_i = \frac{M_{tot} E_i}{(M_{tot} - m_i) E_K}. \tag{19}$$

If one instead chooses to keep the triangle equilateral, the allowed energy fractions restrict data points to an ellipse instead of a circle, and the events can be plotted using barycentric coordinates.

5 Mutual neutralisation of HeH^+ and D^-

5.1 Method

Two sets of MN experiments with ion collisions at center-of-mass energy around 0 eV were conducted at the DESIREE facility. In the first experiment, the MN of HeH^+ and D^- was examined through collisions at ∼0 eV. The deuterium anions were produced in a SNICS ion source and guided through the injection site on the symmetric storage ring. The current of the ion beam was continuously measured while voltages applied to electromagnetic elements were adjusted. This was done in order to optimize the beam and reduce the inevitable loss of ions during each revolution. The positive helium hydride ions were produced in an ECR ion source and injected into the asymmetric storage ring where the same optimization process was repeated.

Once optimized, the D^- and HeH^+ beam currents were measured to be 25.7 nA and 0.7 nA with energies $E_{D^-} = 6.001$ keV and $E_{HeH^+} = 16.732$ keV, respectively. With the intent of minimizing fringe field effects occurring at the outermost sections of the merging region, the decision was made to apply the bias voltage over drift tubes 2, 3 and 4. The bias voltage needed to lower the center-of-mass energy to ∼0 eV was calculated using eq. (8) to 522.5 V and set as an initial value. Subsequently, the voltage was adjusted while taking continuous measurements of the number of reaction products. The maximum number of detections was achieved while applying a bias voltage of 520 V. The time interval between each injection of ions is referred to as the cycle length and was set to 11.4 s.

Data was collected using an imaging detection system that captured neutral products traveling parallel to the ion beams. To identify the MN events in the data, a number of selection criteria were set. These criteria included requirements set on coincidence, detection size, and the intensity of each detection. The primary goal of the data analysis was to determine the kinetic energy release and the energy distribution between the neutral products, more about the data analysis can be found in Sec. 4. Results from the data analysis were later compared to theoretical models of ionic potential curves with the intention of identifying compatible transitions and channels.

5.2 Result and discussion

5.2.1 Three product analysis

The detections identified through data processing as three coincident products from MN of HeH^+ and D^- are shown in Fig. 9. Each dot represents the position of an atom hitting the detector, where H is in red, D in green, and He in blue. It appears clearly that H, with the smallest mass, reaches the furthest out, and He, as the heaviest element, stays closer to the beam center, illustrating the underlying conservation of energy and momentum.

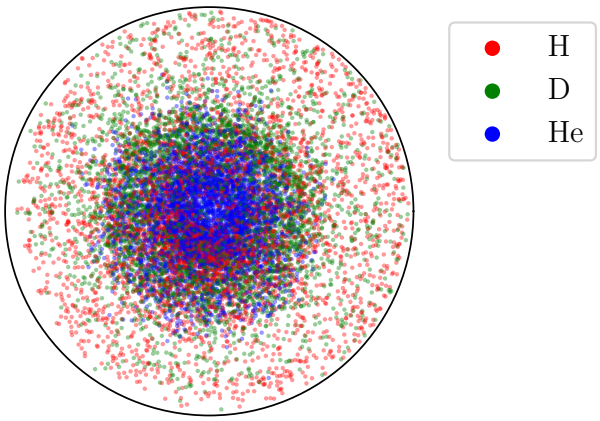

Figure 9 – Illustration of the positions of all the particles identified as MN products on the detector; with H in red, D in green, and He in blue.

Results from the three product analysis of the energy distribution from the MN of HeH^+ and D^- are presented in Fig. 10. A narrow peak is seen at ∼1 eV and a broad peak around 2–6 eV.

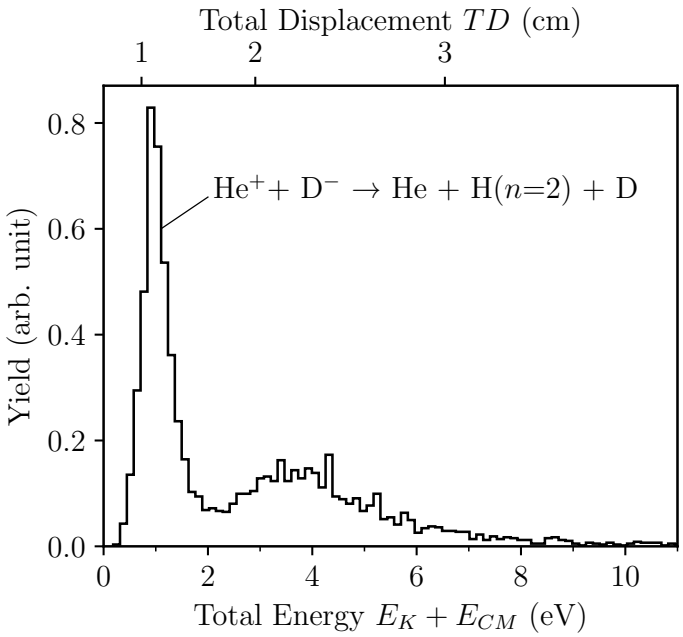

Figure 10 – Total energy and total displacement TD distributions from the three product analysis of HeH^+ / D^-. Most noticeable is a sharp peak at ∼1 eV resulting from the He + H($n = 2$) + D products, and a broad peak at 2–6 eV.

The final quantum states of the products related to the sharp 1 eV peak can directly be identified as He + H($n = 2$) + D, with He and D in their ground states, as presented in Sec. 2.3.1. The distribution of kinetic energy configurations is represented in a Dalitz plot in Fig. 11. A high-density region in the top part of the graph

is the most prominent feature, indicating a high frequency of events with energy configurations where D gains its maximum energy. Another feature of interest is the slight density increase seen alongside the top left border of the ellipse. This region corresponds to events where He reaches its maximum energy. A less prominent feature can be seen in the region around $E_{\mathrm{D}} \approx 0.1$–$0.3\,E_{\mathrm{K}}$, $E_{\mathrm{H}} \approx 0.4$–$0.7\,E_{\mathrm{K}}$, and $E_{\mathrm{He}} \approx 0.15$–$0.4\,E_{\mathrm{K}}$.

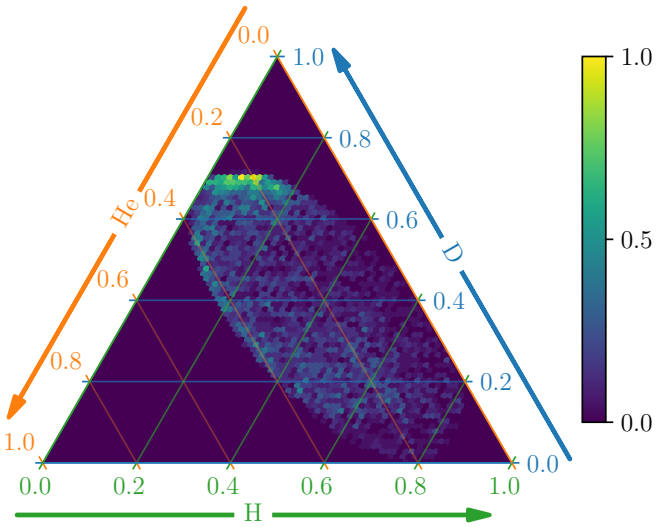

Figure 11 – A Dalitz plot representing the kinetic energy distribution between the three neutral products resulting from $\mathrm{HeH}^+ + \mathrm{D}^- \rightarrow \mathrm{He} + \mathrm{H} + \mathrm{D}$. The maximum allowed kinetic energy release between products of different masses constrains each configuration to lay within an ellipse. A high concentration of events can be seen in the top portion of the distribution towards the maximum energy for D, indicating a large portion of events being a sequential break-up via electron transfer.

5.2.1.1 The energy peak at ∼1 eV

An analysis of the sharp peak around 1 eV is shown in Fig. 12 where a Dalitz plot is presented along with graphs of the fractional energy obtained by each product. Interestingly, the high-density region where D has its maximum energy, visible for all events in Fig. 11, remains prominent after restricting data to $E_K \approx 1\,\mathrm{eV}$. This indicates a sequential break-up via electron transfer. As the products obtained with the 1 eV channel are He, H($n = 2$) and D, the process can be identified as

$$\mathrm{HeH}^+ + \mathrm{D}^- \longrightarrow \mathrm{HeH}^* + \mathrm{D} \longrightarrow \mathrm{He} + \mathrm{H}(n = 2) + \mathrm{D}.$$

This channel is illustrated by the violet arrows in Fig. 13. We expect the intermediate HeH^* to be in the C $^2\Sigma^+$ state since vibrational levels with $v \geq 3$ are a few meV above the dissociative level and can therefore tunnel out to He + H($n = 2$).

The theoretical energy configuration for this break-up is $E_{\mathrm{D}} = 0.7133\,E_{\mathrm{K}}$, with the remaining energy being shared between He and H. A generally good agreement is found between the theoretical configuration and the experimentally obtained results. The measured fractions are shown in Fig. 12 with a pink inset that highlights the

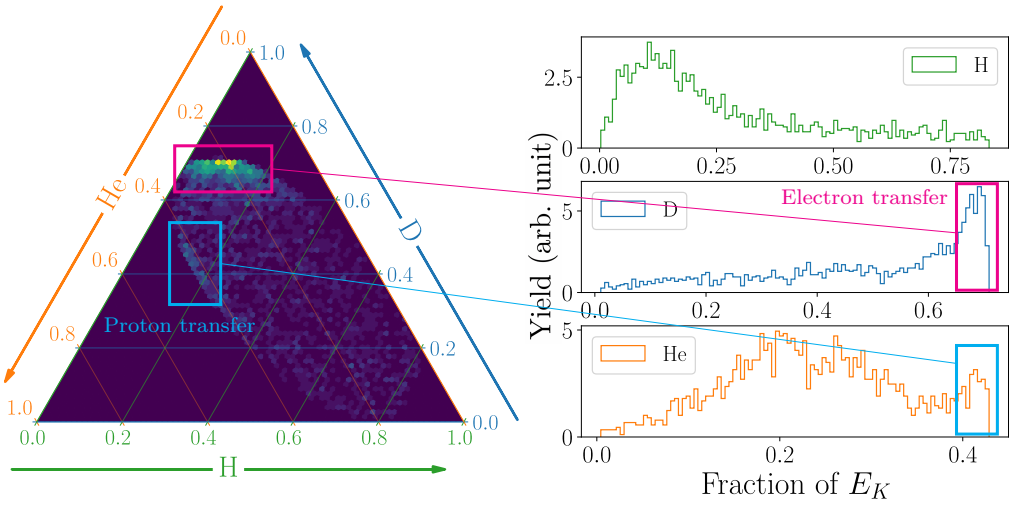

Figure 12 – Normalized energy distribution between the neutral products for the sharp peak at 1 eV. Sequential break-up via electron transfer is the dominating process for MN of HeH^+ / D^- as is shown by the highlighted regions as pink (maximum fractional energy of D). MN via proton transfer occurs less frequently but is responsible for the increase at high fractional energy for He.

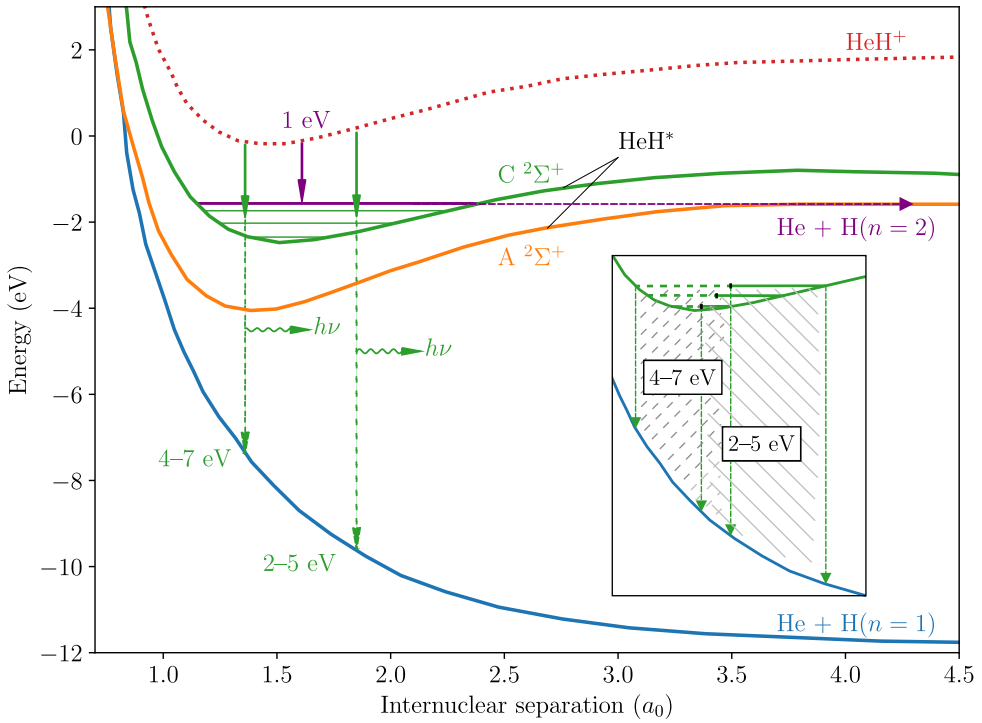

Figure 13 – Potential energy curves for HeH and the HeH^+ cation as a function of internuclear separation. The violet arrows represent the channel corresponding to the 1 eV kinetic energy channel. In green are represented deexcitations from the C $^2\Sigma^+$ state with $E_K = 4$–7 eV for the left side and $E_K = 2$–5 eV for the right side of the potential.

energy fraction for D and the associated region in the Dalitz plot. The spread observed in the energy fraction obtained by D can result partially from the fact that several vibrational levels of the HeH^* ($C\ ^2\Sigma^+$) state are populated, leaving a second contribution to the energy release to He and H of a few meV during tunneling.

A second region of interest in Fig. 12 is a thin, less intense portion of the Dalitz plot where He gets its maximum energy. The grouping in this region is more evident in the energy fraction curve of He, where a peak is formed around its maximum. These events indicate a less significant but still noticeable fraction of MN occurring via proton transfer. The sequential break-up for this second channel is

$$HeH^+ + D^- \longrightarrow He + HD^* \longrightarrow He + H(n = 2) + D.$$

The proton transfer generates neutral He and HD^* that should be in a highly vibrationally excited state which can dissociate rapidly.

5.2.1.2 The broad 2–6 eV energy peak

The channels that can be responsible for the broad peak at 2–6 eV have been investigated and are presented below but more data and further analysis would be required to reach a conclusion for this region of the energy output. The normalized energy distribution for the lower and upper halves of the 2–6 eV region are presented separately in Figs. 14 and 15 as each presents different features. Splitting at 4 eV corresponds to the upper limit of the broad peak, potentially indicating processes occurring on different sides of a potential curve.

A process that naturally generates a continuous distribution of energy release, as the one seen in the 2–6 eV region, is vertical transitions via photon emission from an excited state to a dissociative state. Looking at the potential energy curves of HeH for electron transfer, a channel to the HeH ground state, dissociating to He + $H(n = 1)$ is one possibility. For proton transfer, the dissociative state could be the doubly excited HD^{**} ($b\ ^3\Sigma_u^+$) state leading to D + $H(n = 1)$.

To better understand this process, the fractional energies acquired by the neutrals can be evaluated and reveal more information. These calculations are used as a first tool to guide us and determine whether or not deexcitation through photon emission is interesting to investigate further. In the case of electron transfer, deexcitations from the HeH^* ($A\ ^2\Sigma^+$) and HeH^* ($C\ ^2\Sigma^+$) states to the ground state have been investigated. For proton transfer, we looked at transitions from HD* ($B\ ^1\Sigma_u^+$) to the HD^{**} ($b\ ^3\Sigma_u^+$) dissociative state. Estimates of the measured E_K, photon energy E_γ, and fractional energies are presented in Table 3. Deexcitations from the left and right portions of the potential curves were calculated separately. For instance, "$C\ ^2\Sigma^+$ left" in the table indicates deexcitations from all vibrational levels in the $C\ ^2\Sigma^+$ curve, between the utmost left limits and halfway to the right, as is visualized in the inset in Fig. 13.

In Fig. 14, presenting data between 2–4 eV, we see a denser region mostly delimited by $0.15 < E_D/E_K < 0.35$. But a broad continuous distribution emerges almost across all allowed fractional energies for the other two products. In Fig. 15, with

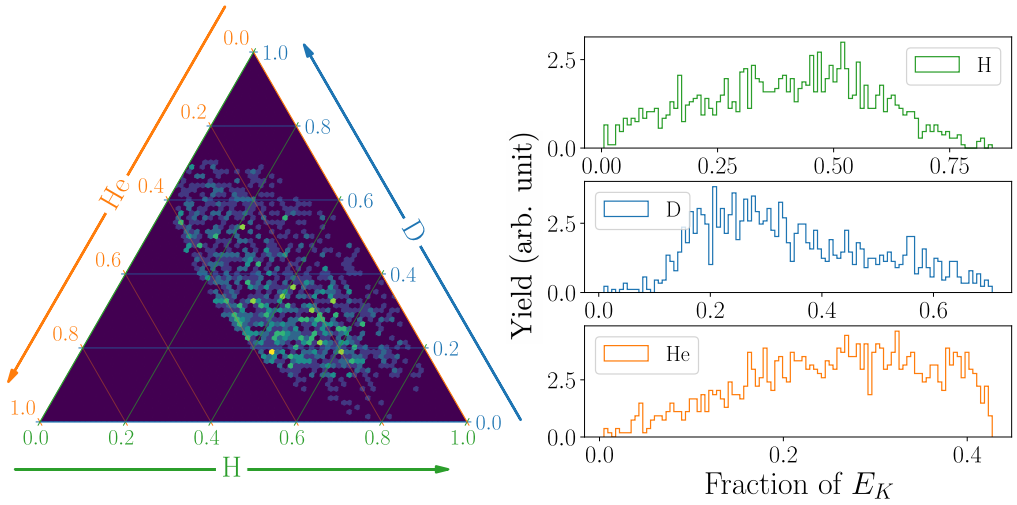

Figure 14 – Normalized energy distribution between the 3 neutral products for events with $2\,\text{eV} < E_K < 4\,\text{eV}$.

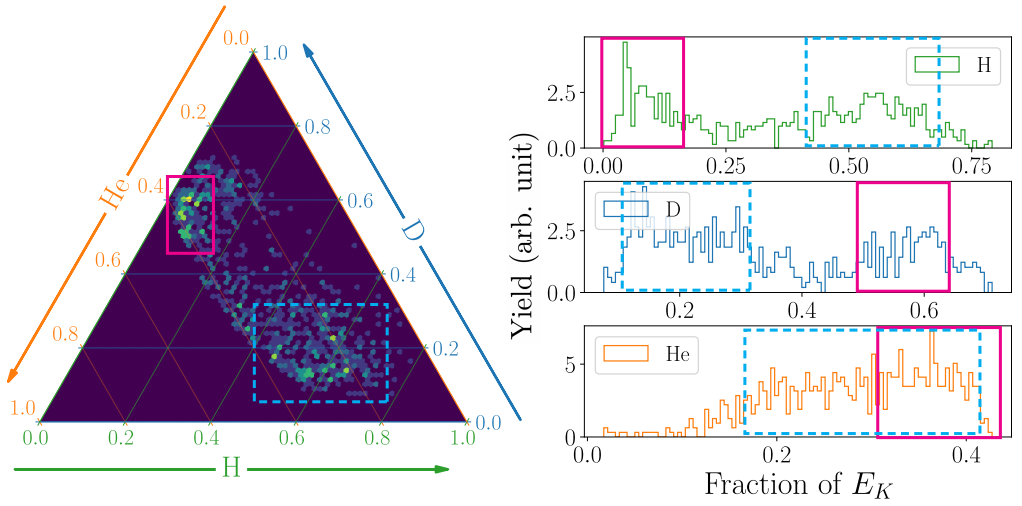

Figure 15 – Normalized energy distribution between the 3 neutral products for events with $E_K > 4\,\text{eV}$.

Table 3 – Expected ranges of energies and fractional energies from vertical transitions.

Init. st.	Final st.	E_γ	E_D/E_K	E_{He}/E_K	E_H/E_K	E_K
HeH*	HeH					
C $^2\Sigma^+$ left	X $^2\Sigma^+$	4–7 eV	0.10–0.23	0.02–0.41	0.36–0.84	4–7 eV
C $^2\Sigma^+$ right	X $^2\Sigma^+$	6–9 eV	0.19–0.31	0.00–0.43	0.27–0.79	2–5 eV
A $^2\Sigma^+$ left, $v = 0$–4	X $^2\Sigma^+$	1–7 eV	0.12–0.31	0.00–0.43	0.27–0.85	4–10 eV
A $^2\Sigma^+$ left, $v = 5$–8	X $^2\Sigma^+$	1–9 eV	0.07–0.27	0.00–0.42	0.31–0.85	2–5 eV
A $^2\Sigma^+$ right, $v = 0$–4	X $^2\Sigma^+$	4–8 eV	0.27–0.44	0.00–0.43	0.13–0.72	3–7 eV
A $^2\Sigma^+$ right, $v = 5$–8	X $^2\Sigma^+$	7–10 eV	0.27–0.52	0.00–0.42	0.07–0.73	2–5 eV
HD*	HD**					
B $^1\Sigma_u^+$	b $^3\Sigma_u^+$	1–8 eV	0.00–0.71	0.08–0.28	0.02–0.85	3–10 eV

$E_K > 4\,\text{eV}$, two clusters seem to appear, this is highlighted as solid pink and dotted blue.

We can now compare the distributions with the calculations. In Table 3, we can see that transitions from the right portion of the HeH^* ($C\ ^2\Sigma^+$) curve imply $0.19 < E_D/E_K < 0.31$ and $2\,\text{eV} < E_K < 5\,\text{eV}$. These limits appear to be appropriate to generate the pattern seen in Fig. 14. The higher vibrational states, $v = 5$–8, of the $A\ ^2\Sigma^+$ curve could also be contributing, even if the bounds from the calculations seem a bit too large. These high vibrational levels in the $A\ ^2\Sigma^+$ state lie around the same potential energies as the levels of the $C\ ^2\Sigma^+$ state but are wider. If the $A\ ^2\Sigma^+$ state contributed noticeably, E_D/E_K should have these same broader limits. Since this does not seem to be the case, we assume that most deexcitations take place from the $C\ ^2\Sigma^+$ state.

In Fig. 15, the region highlighted as dotted blue is similar to the one we just discussed, but with approximately $0.10 < E_D/E_K < 0.20$. These bounds seem to correspond to transitions from the left portion of the $C\ ^2\Sigma^+$ state. It is particularly difficult to distinguish the bounds of this region. Even though other states could be contributing, we definitely need more data for this analysis.

Lastly, the region highlighted as solid pink in Fig. 15 cannot be matched with any of our calculations and remains to be coupled with the appropriate reaction process.

To summarize, the most probable contribution to the broad 2–6 eV energy peak is thought to be the result of deexcitations from the HeH^* ($C\ ^2\Sigma^+$, $v = 0, 1, 2$) states as shown by the green arrows in Fig. 13. Vertical transitions after proton transfer do not seem to be occurring.

Moving forward, we suggest performing simulations for vertical transitions between the HeH^* ($A\ ^2\Sigma^+$ and $C\ ^2\Sigma^+$) states, and the HeH ($X\ ^2\Sigma^+$) state, accounting for the cumulative effect of all vibrational states.

5.2.2 Two product analysis

MN reactions that involve only two products are, in principle, easier to analyze. However, when two product analysis is performed on data where three products are also present, more steps are needed. Because of the sensitivity of the detector, there is a risk that a fraction of the three products only generate two hits. This would be the case when one of the products does not trigger a new detection, for instance, if the saturation from the previous detection is still over the threshold intensity. In this case, the event will appear on the two-product spectrum and not on the three-product spectrum. Furthermore, when most of the energy is shared between two products, the center of mass will appear centered even if only these two products are detected. This means that such events survive the center of the mass cut, and the total energy will match the corresponding energy of the three products.

To filter out the three product backgrounds, we assume that the third detection would be the one missing, and we generate the corresponding energy spectrum from the three product dataset. Since our experiment can generate both HeH + D and HD + He as two products, we present both cases. In Figs. 16 and 17, on the left

panels, the two product analysis is shown in dashed blue, superimposed with the three product background in solid black. On the right panels, the background has been subtracted, and what we see should be the result of the actual two-product MN.

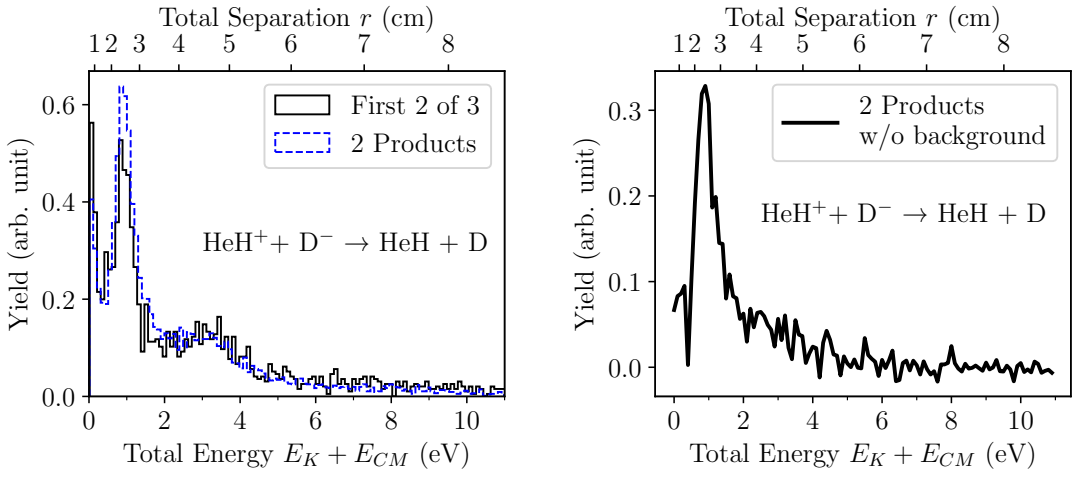

Figure 16 – Analysis of the total energy and separation for the MN of HeH^+ and D^- resulting in HeH + D. On the left, the energy spectrum from the two product analysis is shown in dashed blue, and the background generated from three products where the last product is not detected is shown in solid black. After subtracting the three product backgrounds, we obtain the spectrum shown on the right.

A sharp peak at ∼1 eV appears as a result of electron transfer, as seen in Fig. 16. This would indicate that some excited HeH^* reached the detector before dissociation. In the merging region, the ions travel approximately at $v \approx 790\,245$ m/s. With an average distance of $L = 1.7685$ m to the detector, the time of flight is about $t \approx 2\,\mu$s. But, the estimated lifetime of the excited states of HeH is only about 10–45 ns [26]. The fact that the HeH^* would reach the detector before dissociating is therefore unexpected. Consequently, there is no predicted channel with $E_K = 1$ eV and two products. Although, the channel responsible for the three products assumes tunneling from HeH^* ($C\ ^2\Sigma^+$, $v \geq 3$), which could take time. Secondly, the appearance of the peak is highly dependent on how the subtraction of the background is made. And the latter needs sufficiently large data sets to be reliable, which might not be the case.

From the analysis of proton transfer presented in Fig. 17, a sharp peak at 1 eV and a broad peak at 1.5–6 eV are visible. These would suggest that not all HD^* dissociate before detection. Even though there is a slight peak at 1 eV, its intensity varies greatly depending on different choices made on the subtraction of the background. And this process is, here again, too sensitive to the size of the dataset to be reliable. We, therefore, suspect that the 1 eV peak most likely is the result of background from other processes. In contrast to HeH, the HD^* ($B\ ^1\Sigma_u^+$) state (see Fig. 2) does not require tunneling before dissociation. We cannot, therefore, explain how a channel at 1 eV with HD^* + He would take place. The broad peak at 1.5–6 eV could result

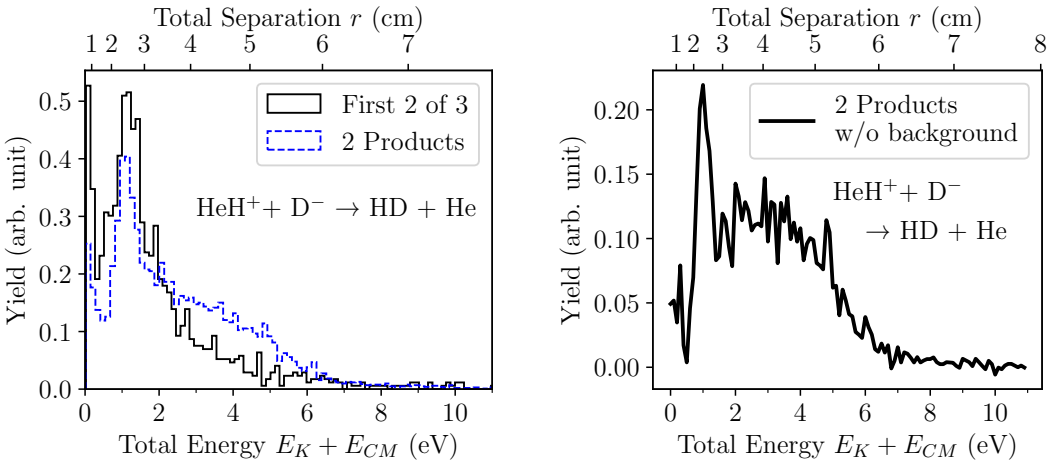

Figure 17 – Analysis of the total energy and separation distributions for the two products HD + He. On the left, the two product spectrum is shown in dashed blue, and the background resulting from three products with the last one missing the detector is shown in solid black. We obtain, after subtracting the background, the spectrum shown on the right. A sharp peak appears at 1 eV and a broad peak at 1.5–6 eV.

from MN to lower vibrational states of HD* (B $^1\Sigma_u^+$) but they would only generate up to $E_K \approx 4$ eV. Additionally, we expect fewer detections for three products when reaching higher energies. This generates an under-representation of the events at higher energies and could be responsible for the broad peak. This feature might subsequently also be the result of background, and needs to be further analyzed.

5.2.3 General observations

One of the main advantages of performing the experiment at DESIREE is the extremely low temperature at which the ions circulate for long storage times, allowing for internal cooling. The HeH^+ ion in its ground state has vibrational states that have lifetimes of up to 120 ms [27]. These were expected to be populated at the time of injection. Because of their short lifetime, the effect of this cooling is observable since MN from a higher vibrational state will release slightly more energy and create more noise in the continuous part of the energy output. Both effects are clearly visible in Fig. 18 where we see the dashed red line shifted towards higher energies and an almost non-existent second peak. In solid blue, the cooled ions create instead a sharp and symmetric peak at ∼1 eV and a continuous broad peak at 2–6 eV. Several factors are responsible for the broadening of the sharp peak. The main contribution comes from the length of the interaction region, generating uncertainty in the exact position of the MN reaction. All reactions are assumed to take place in the middle of the biased region in our analysis, leading to a statistical uncertainty of about 6.6%. Broadening can also be the result of the two ion beams not being completely parallel but having a small incident angle. Fig. 19 shows the distribution of neutral particle positions on the detector giving a visual representation of the beam overlap. The oval-shaped distribution indicates imperfect ion beam alignment which might affect the total count rate and create a systematic uncertainty. Finally, different velocities

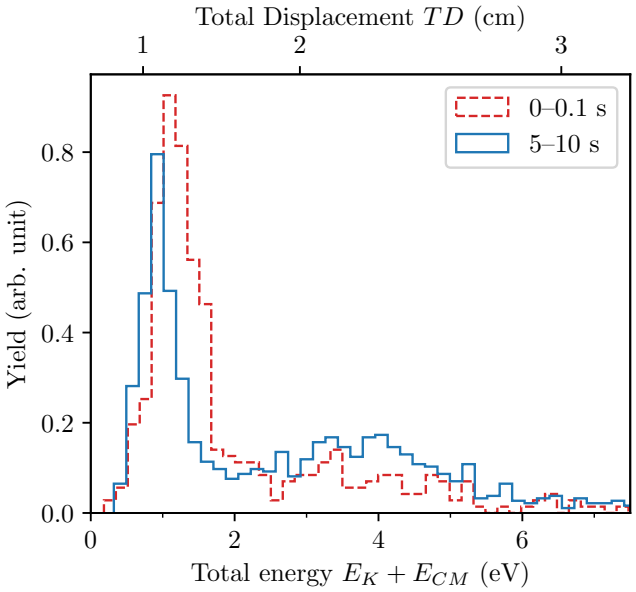

Figure 18 – Normalised number of events plotted against the total energy released. Cooling effects are illustrated through a comparison of detections made during the first 0.1 s after injection (dashed red) and detections made between 5 and 10 s after injection (solid blue).

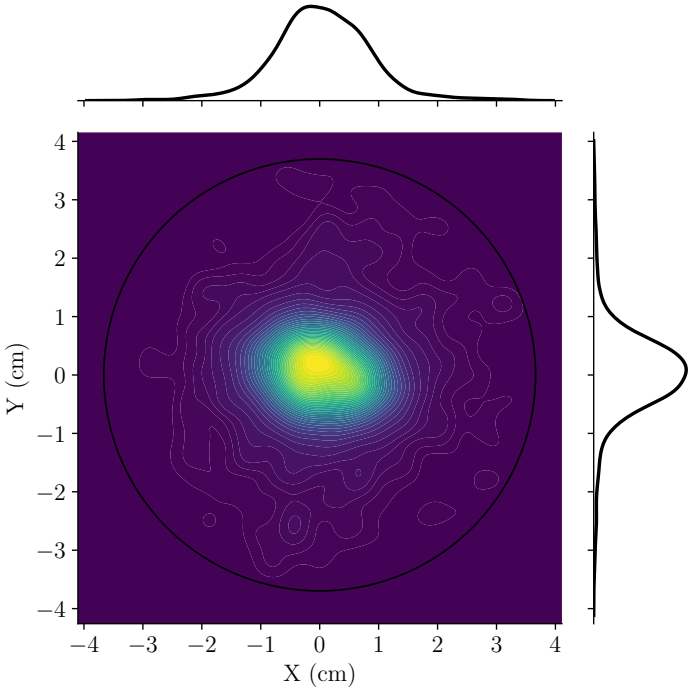

Figure 19 – Density plot showing the position of detected mutual neutralisation products. The imposed circle illustrates the physical size of the detector sensor. This illustrates the spread and overlap of both ion beams.

of the beams can, because of the length of the interaction region, also broaden the energy peaks. The instrumental setup at DESIREE allows only the total energy of the particles to be measured. The center of mass energy E_{CM} has to be estimated by looking at the shift in energy between the predicted kinetic energy release and the measured value obtained with curve fitting. Without performing this accurate estimation, E_{CM} appears to be no higher than 200 meV, the predicted kinetic energy release being $E_K = 0.8\,\text{eV}$, but curve fitting would give a better value.

Although the goal of the experiments with the merged beam section at DESIREE is to reach zero collision energies, very low collision energy cannot be avoided. This can be caused by a limitation in the voltage applied in the biased region as well as the fringe effect from both ends. The fringe effect is visible in Fig. 18, where we see some counts with slightly higher energy, broadening the main peak towards the right.

6 Mutual neutralisation of Na^+ and Si^- with manipulated quantum levels

6.1 Method

The second experiment aimed to test the ability to selectively manipulate quantum states in stored ions. When performing MN experiments, the measured kinetic energies result from collisions occurring between all the populated states. While most anions have only one stable ground state, some have a long-lived metastable excited state. Since ion sources produce ions in a wide distribution of energies, different metastable states are often populated in the ion beams. Any population of metastable states with a lifetime longer than the storing capabilities of DESIREE will then be present while performing experiments. There is therefore a need to investigate the possibility to deplete the negative ion beam of the excited state, thus allowing studies on ground state ions. To investigate this method, we chose the silicon Si^- anion due to its long-lived metastable ^2D state. With a binding energy of $\sim 0.52\,\text{eV}$, the ^2D state can be photodetached using an IR laser. The positive sodium ion Na^+ was chosen as the colliding cation because of its similar mass and its low ionization potential. The distinct channels related to MN with both Si^- states are expected to be clearly visible thanks to the simple electron configuration of Na^+. The development of this method, if successful, will allow for astrophysical systems to be studied in this way in future experiments.

The Si^- ions were produced in a SNICS ion source and the Na^+ were produced in a Nielsen ion source. The Si^- ion, although being the heavier of the two ions, was stored in the symmetric ring by reason of its superior storing capabilities. This allowed for a longer duration of the laser depletion. The Si^- and Na^+ beam energies were 10.0 keV and 9.008 keV respectively. The collision energy was brought to $\sim$0 eV in sections 2, 3 and 4 of the merging region by applying a bias voltage of 470 V.

A 5.7 W laser was mounted co-linearly with the injection point of the symmetric ring (see Fig. 6) to carry out the depletion of the ^2D state in Si^-. The time between ion injections was set to 63 s (60 s of data collection and 3 s for resetting the experiment).

Measurements of the neutral products resulting from MN events between Si^- and Na^+ were subsequently taken, both before and after depletion. The effect of manipulating the quantum states of Si^- was examined by comparing the energy distribution and channels observed from MN before and after depletion.

6.2 Result and discussion

Fig. 20 shows the resulting energies from MN of Na^+ and Si^- without depletion of the excited Si^- ions. The four expected channels are

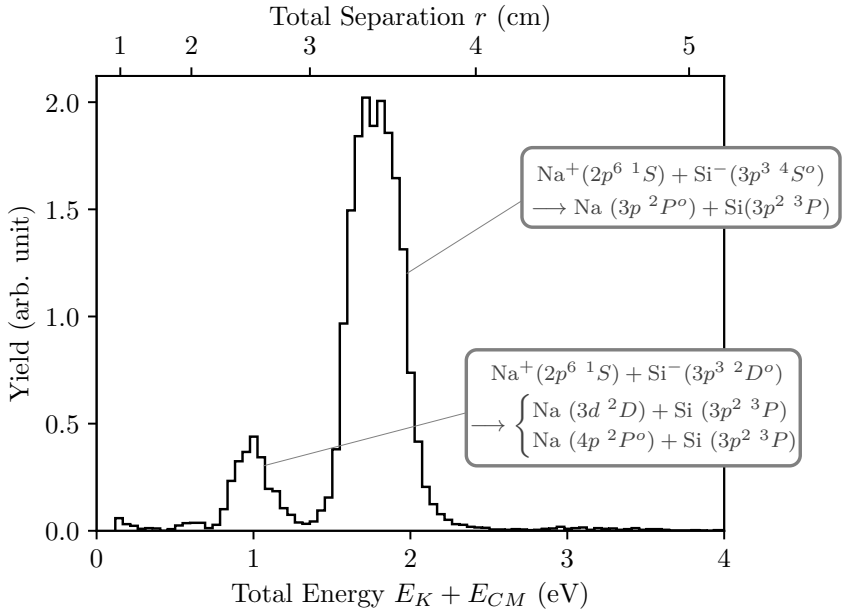

Figure 20 – Yield as a function of total energy $E_K + E_{CM}$ and total separation r for the MN of Na^+ and Si^-. Two distinct peaks are visible at $E_K + E_{CM} \approx 1.7\,\mathrm{eV}$ and $E_K + E_{CM} \approx 1\,\mathrm{eV}$.

$$\begin{aligned}
\mathrm{Na}^+(2p^6\ ^1S) + \mathrm{Si}^-(3p^3\ ^4S^o) \quad &\rightarrow \quad \mathrm{Na}\ (3p\ ^2P^o) + \mathrm{Si}\ (3p^2\ ^3P) && 1.6504\,\mathrm{eV} \\
\mathrm{Na}^+(2p^6\ ^1S) + \mathrm{Si}^-(3p^3\ ^2D^o) \quad &\rightarrow \quad \begin{cases} \mathrm{Na}\ (3d\ ^2D) + \mathrm{Si}\ (3p^2\ ^3P) & 0.9991\,\mathrm{eV} \\ \mathrm{Na}\ (4p\ ^2P^o) + \mathrm{Si}\ (3p^2\ ^3P) & 0.8630\,\mathrm{eV} \\ \mathrm{Na}\ (5s\ ^2S) + \mathrm{Si}\ (3p^2\ ^3P) & 0.4997\,\mathrm{eV}. \end{cases}
\end{aligned}$$

A dominant peak can clearly be identified at $E_K + E_{CM} \approx 1.7\,\mathrm{eV}$ ($r \approx 3.5\,\mathrm{cm}$), which corresponds to the $\mathrm{Na}^+(2p^6\ ^1S) + \mathrm{Si}^-(3p^3\ ^4S^o) \rightarrow \mathrm{Na}(3p\ ^2P^o) + \mathrm{Si}(3p^2\ ^3P)$ channel with a predicted energy release of 1.6504 eV. A secondary peak is visible around $E_K + E_{CM} \approx 1\,\mathrm{eV}$ ($r \approx 2.5\,\mathrm{cm}$) which lies within the predicted energy of the $\mathrm{Na}^+(2p^6\ ^1S) + \mathrm{Si}^-(3p^3\ ^2D^o) \rightarrow \mathrm{Na}(3d\ ^2D) + \mathrm{Si}(3p^2\ ^3P)$ channel as well as the $\mathrm{Na}^+(2p^6\ ^1S) + \mathrm{Si}^-(3p^3\ ^2D^o) \rightarrow \mathrm{Na}(4p\ ^2P^o) + \mathrm{Si}(3p^2\ ^3P)$ channel. Due to the proximity of these channels and the limitations of our energy resolution, we interpret both channels to be contributing to the peak. We did not detect the presence of the 0.5 eV channel expected from $\mathrm{Na}^+(2p^6\ ^1S) + \mathrm{Si}^-(3p^3\ ^2D^o) \rightarrow \mathrm{Na}(5s\ ^2S) + \mathrm{Si}(3p^2\ ^3P)$.

The investigation of the impact of laser depletion of the $\mathrm{Si}^-(^2D^o)$ state on mutual neutralisation products is shown in Fig. 21. Here, the channel ratio without depletion is compared to the ratio observed after depleting the Si^- ion beam for 30 s at 5.7 W, aiming at leaving Si^- in the $^4S^o$ ground state only. The figure shows a noticeable decrease in detections around 1 eV for the depleted beam. In order to distinguish the impact of laser depletion from spontaneous deexcitation of excited

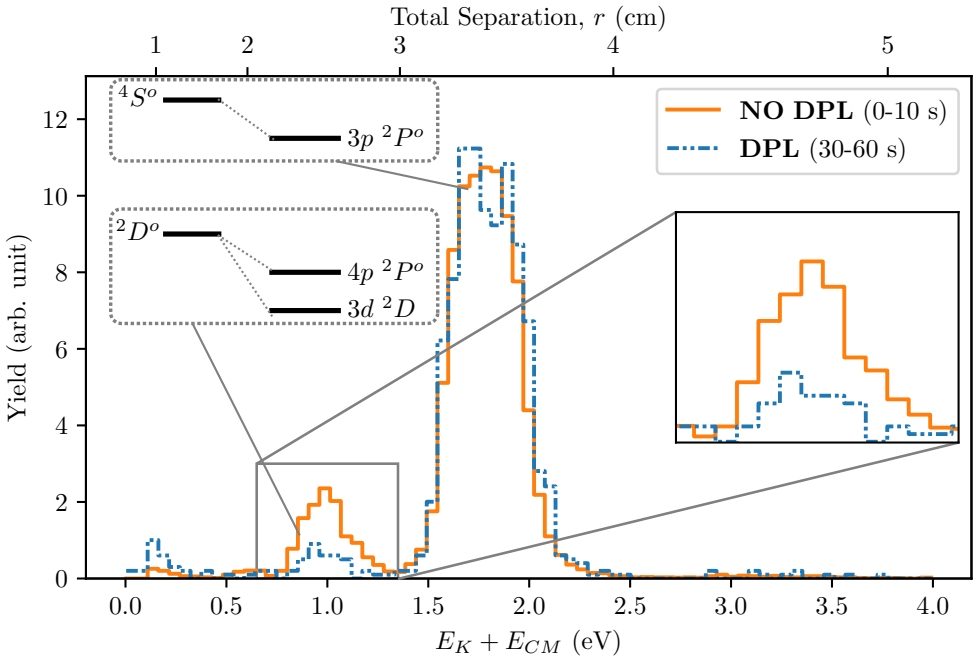

Figure 21 – Yield of neutral products as a function of total energy $E_K + E_{CM}$. The solid orange line represents the outcomes of MN events conducted with a 10 s cycle length without depletion. Results from MN events after 30 s of depletion with a 5.7 W laser are shown in dotted blue. The zoomed inset highlights the peak corresponding to transitions from the excited $^2D^o$ state in Si^- to the $4p\ ^2P^o$ and $3d\ ^2D$ states in Na. A noticeable but incomplete reduction in the yield is observed in this region after depletion was performed.

$Si^-(^2D^o)$ ions, further analyses were made on data from MN with a 60 s cycle time and without laser depletion. In Fig. 22, the data gathered during the first 10 s of each ion beam cycle is compared to the data gathered in the last 30 s of the cycles. The increased storage time shows no clear impact on any of the observed channels. We thus infer that the spontaneous radiative deexcitation of $Si^-(^2D^o)$ has no significant impact on the distribution of products over time and the $Si^-(^2D^o)$ state is therefore long-lived. When combined with the results in Fig. 21, these results suggest that the depletion process successfully reduced the population of excited states in the Si^- beam. Another interesting and somewhat surprising result is that the channel resulting from the metastable $^2D^o$ state remains visible after 30 s of depletion. This result may be explained by a low depletion rate caused by insufficient overlap between the laser beam and the Si^- ion beam, or insufficient laser power. Another possible explanation is that there might be other channels that generate $E_K \approx 1$ eV. The ions inherit a wide range of energies after production which makes the presence of excited ions possible. It is then conceivable that some excited Na^{+*} ions were present, opening new channels,

$$\mathrm{Na}^{+*} + \mathrm{Si}^- \longrightarrow \mathrm{Na}^{**} + \mathrm{Si} \longrightarrow \mathrm{Na}^+ + \mathrm{Si} + \mathrm{e}^-$$
$$\mathrm{Na}^{+*} + \mathrm{Si}^- \longrightarrow \mathrm{Na}^{**} + \mathrm{Si} \longrightarrow \mathrm{Na}^* + \mathrm{Si} + h\nu.$$

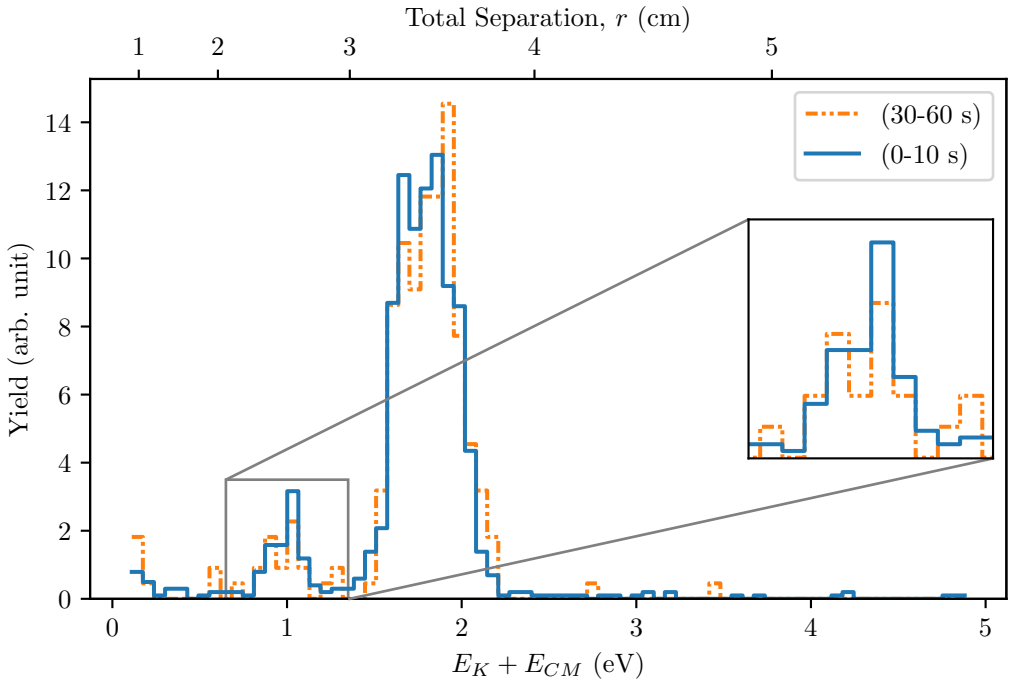

Figure 22 – Yield as a function of total energy $E_K + E_{CM}$ and total separation r. Comparison of the total energy distribution during the first 10 s after injection (solid blue) and the last 30 s of the cycle (dotted orange). The zoomed inset highlights the region corresponding to channels from excited Si^- ($^2D^o$) states. No cooling effect can be observed.

If this was the case, MN would lead to a doubly excited neutral atom, Na^{**}. If this product auto-ionizes, it would continue to be deflected in the storage rings and not be detected. But Na^{**} could also deexcite through photon emission and meet the detector. The second outcome, if releasing the appropriate kinetic energy, would be registered at around 1 eV, which would account for the observed persistence of this peak.

For the prominent peak at $E_K + E_{CM} \approx 1.7$ eV, no observable change was detected after depletion. This is to be expected since the dominant channel stems from MN of ground state Na^+/Si^- ions and should therefore not be affected by the depletion.

A suggestion for future improvement is to analyze the distribution of states that are populated in the ion beams.

7 Conclusion

The experiments conducted at DESIREE in Stockholm aimed to determine the final quantum states of mutual neutralisation experiments and perform a proof of principle experiment involving the manipulation of the quantum state population in ion beams through laser depletion.

For the MN of HeH^+ and D^-, the main result is the presence of the $HeH^+ + D^- \rightarrow He + H(n = 2) + D$ channel that was observed as a peak at $E_{CM} + E_K \approx 1\,\text{eV}$. This agrees with the theoretical value of $E_K = 0.8020\,\text{eV}$. The $HeH^+ + D^- \rightarrow HeH^*(C\ ^2\Sigma^+) + D \rightarrow He + H(n = 1) + h\nu + D$ channel is suggested to be the three product channel observed at $E_{CM} + E_K \approx 2$–$6\,\text{eV}$. The analysis performed here cannot rule out two product channels and we could not come to a definite conclusion. We, therefore, suggest further investigation of the two-product energy spectrum.

Determining the final quantum states from MN reactions is greatly facilitated at DESIREE by both the storage and cooling capabilities. The areas of uncertainty remaining include the energy loss during radiative processes. Additional detectors capable of measuring the photon energies would be a great addition to the current setup. Measurements of photons emitted as a consequence of MN would be a natural progression to this experiment. Combining the results obtained during this experiment with measurements of emitted photons would allow specific transitions occurring by radiative deexcitation to be identified.

The findings of this report contribute to the understanding of neutralisation processes involving helium hydride ions. Further research should be undertaken in order to conclude relevant cross sections and branching ratios for the MN of HeH^+ and D^- and with these gain a better understanding of HeH^+ involvement in the cooling of the early universe.

The MN of Na^+ and Si^- resulted in the observation of three channels. The main peak is identified as the $Na^+(2p^6\ ^1S) + Si^-(3p^3\ ^4S^o) \rightarrow Na(3p\ ^2P^o) + Si(3p^2\ ^3P)$ channel at $E_{CM} + E_K \approx 1.7\,\text{eV}$. The theoretical corresponding value was $1.6504\,\text{eV}$. The lower peak at $E_{CM} + E_K \approx 1\,\text{eV}$ corresponds to the unresolved $Na^+(2p^6\ ^1S) + Si^-(3p^3\ ^2D^o) \rightarrow Na(3d\ ^2D) + Si(3p^2\ ^3P)$ $(0.9991\,\text{eV})$ channel together with the $Na^+(2p^6\ ^1S) + Si^-(3p^3\ ^2D^o) \rightarrow Na(4p\ ^2P^o) + Si(3p^2\ ^3P)$ $(0.8630\,\text{eV})$ channel. The predicted $Na^+(2p^6\ ^1S) + Si^-(3p^3\ ^2D^o) \rightarrow Na(5s\ ^2S) + Si(3p^2\ ^3P)$ channel was not observed.

After performing depletion of the $Si^-(^2D^o)$ state with a 5.7 W laser, we were able to observe a decrease in the number of counts in both channels emanating from MN involving the excited $Si^-(^2D^o)$ ions. Experimental data gathered in the first 10 s of each cycle was compared against data gathered in the last 30 s of each cycle in order to examine the effects of radiative deexcitation from excited $Si^-(^2D^o)$ ions. As no significant effect was observed from radiative deexcitation, the incomplete effect of laser depletion remains unexplained.

Acknowledgements

We express our sincere gratitude to our supervisor Prof. Dag Hanstorp for his endless enthusiasm and passion to share his knowledge. Dag works tirelessly to facilitate projects and connect physics students over the world and he is the reason this project was made possible. We would also like to thank Mathias Poline, PhD student, and Dr. Arnaud Dochain for their expertise, insights, and guidance. All the many hours of discussions and new ideas to be tested have been invaluable while scratching the surface of this fascinating research field. Lastly, we would like to acknowledge Stockholm University and the whole team at DESIREE for welcoming us and making us feel like part of the research team.

References

[1] S. Lepp, P. C. Stancil, and A. Dalgarno. "Atomic and molecular processes in the early Universe". In: *Journal of Physics B: Atomic, Molecular and Optical Physics* 35.10 (May 2002), R57. ISSN: 0953-4075. DOI: 10.1088/0953-4075/35/10/201. URL: https://dx.doi.org/10.1088/0953-4075/35/10/201.

[2] Rolf Güsten et al. "Astrophysical detection of the helium hydride ion HeH+". In: *Nature* 568.7752 (Apr. 2019). Number: 7752 Publisher: Nature Publishing Group, pp. 357–359. ISSN: 1476-4687. DOI: 10.1038/s41586-019-1090-x. URL: https://www.nature.com/articles/s41586-019-1090-x.

[3] Elodie A. Engel et al. "Calculated spectra for HeH^+ and its effect on the opacity of cool metal-poor stars". In: *Monthly Notices of the Royal Astronomical Society* 357.2 (Feb. 21, 2005), pp. 471–477. ISSN: 0035-8711. DOI: 10.1111/j.1365-2966.2005.08611.x. URL: https://doi.org/10.1111/j.1365-2966.2005.08611.x.

[4] Bovino, S. et al. "Ion chemistry in the early universe - Revisiting the role of HeH^+ with new quantum calculations". In: *A&A* 529 (2011), A140. DOI: 10.1051/0004-6361/201116740. URL: https://doi.org/10.1051/0004-6361/201116740.

[5] Gokul Kannan et al. "Rydberg States of H_3 and HeH as Potential Coolants for Primordial Star Formation". In: *The Journal of Physical Chemistry A* 125.20 (May 27, 2021). Publisher: American Chemical Society, pp. 4267–4275. ISSN: 1089-5639. DOI: 10.1021/acs.jpca.0c10983. URL: https://doi.org/10.1021/acs.jpca.0c10983.

[6] P. C. Stancil and A. Dalgarno. "Chemical processes in astrophysical radiation fields". In: *Faraday Discussions* 109.0 (Jan. 1, 1998). Publisher: The Royal Society of Chemistry, pp. 61–69. ISSN: 1364-5498. DOI: 10.1039/A800074C. URL: https://pubs.rsc.org/en/content/articlelanding/1998/fd/a800074c.

[7] A. Dochain. "Systematic study of mutual neutralization reactions between atomic species using the merged beam method and an asymptotic model". Prom.: Urbain, X. PhD thesis. UCLouvain, Jan. 2022. URL: http://hdl.handle.net/2078.1/263451.

[8] G. Eklund. "Experiments on mutual neutralization using storage rings with merged ion beams". PhD thesis. Stockholm University, Jan. 2020. URL: http://urn.kb.se/resolve?urn=urn:nbn:se:su:diva-187002.

[9] R. von Hahn et al. "The cryogenic storage ring CSR". In: *Review of Scientific Instruments* 87.6 (June 16, 2016), p. 063115. ISSN: 0034-6748. DOI: 10.1063/1.4953888. URL: https://doi.org/10.1063/1.4953888.

[10] Y. Nakano et al. "Design and commissioning of the RIKEN cryogenic electrostatic ring (RICE)". In: *Review of Scientific Instruments* 88.3 (Mar. 27, 2017), p. 033110. ISSN: 0034-6748. DOI: 10.1063/1.4978454. URL: https://doi.org/10.1063/1.4978454.

[11] K. Abrahamsson et al. "CRYRING — a synchrotron, cooler and storage ring". In: *Nuclear Instruments and Methods in Physics Research Section B: Beam Interactions with Materials and Atoms* 79.1 (June 2, 1993), pp. 269–272. ISSN:

0168-583X. DOI: 10.1016/0168-583X(93)95341-2. URL: https://www.sciencedirect.com/science/article/pii/0168583X93953412.

[12] H. T. Schmidt et al. "First storage of ion beams in the Double Electrostatic Ion-Ring Experiment - DESIREE". In: *Review of Scientific Instruments* 84.5 (May 2013), p. 055115. ISSN: 0034-6748, 1089-7623. DOI: 10.1063/1.4807702. arXiv: 1804.00129[physics]. URL: http://arxiv.org/abs/1804.00129.

[13] C. Strömholm et al. "Dissociative recombination and dissociative excitation of $^4HeH^+$: Absolute cross sections and mechanisms". In: *Physical Review A* 54.4 (Oct. 1, 1996). Publisher: American Physical Society, pp. 3086–3094. DOI: 10.1103/PhysRevA.54.3086. URL: https://link.aps.org/doi/10.1103/PhysRevA.54.3086.

[14] Ilya Obodovskiy. "Chapter 11 - Recombination of Charges". In: *Radiation*. Ed. by Ilya Obodovskiy. Elsevier, Jan. 1, 2019, pp. 197–205. ISBN: 978-0-444-63979-0. DOI: 10.1016/B978-0-444-63979-0.00011-2. URL: https://www.sciencedirect.com/science/article/pii/B9780444639790000112.

[15] M. Poline. "Mutual neutralisation reactions in atmospheric and industrial plasmas". Licentiate Thesis. Stockholm University, Nov. 2022. URL: http://urn.kb.se/resolve?urn=urn:nbn:se:su:diva-211349.

[16] Edward P. L. Hunter and Sharon G. Lias. "Evaluated Gas Phase Basicities and Proton Affinities of Molecules: An Update". In: *Journal of Physical and Chemical Reference Data* 27.3 (May 1998), pp. 413–656. ISSN: 0047-2689. DOI: 10.1063/1.556018. eprint: https://pubs.aip.org/aip/jpr/article-pdf/27/3/413/11552089/413_1_online.pdf. URL: https://doi.org/10.1063/1.556018.

[17] Daniel Sprecher et al. "Communication: The ionization and dissociation energies of HD". In: *The Journal of Chemical Physics* 133.11 (Sept. 2010). 111102. ISSN: 0021-9606. DOI: 10.1063/1.3483462. eprint: https://pubs.aip.org/aip/jcp/article-pdf/doi/10.1063/1.3483462/15431464/111102_1_online.pdf. URL: https://doi.org/10.1063/1.3483462.

[18] Michael Scheer et al. "Systematic study of the stable states of C^-, Si^-, Ge^-, and Sn^- via infrared laser spectroscopy". In: *Phys. Rev. A* 58 (4 Oct. 1998), pp. 2844–2856. DOI: 10.1103/PhysRevA.58.2844. URL: https://link.aps.org/doi/10.1103/PhysRevA.58.2844.

[19] R. D. Thomas et al. "The double electrostatic ion ring experiment: A unique cryogenic electrostatic storage ring for merged ion-beams studies". In: *Review of Scientific Instruments* 82.6 (June 2011). Publisher: American Institute of Physics, p. 065112. ISSN: 0034-6748. DOI: 10.1063/1.3602928. URL: https://aip.scitation.org/doi/10.1063/1.3602928.

[20] Mathias Poline et al. "Mutual neutralisation of O^+ with O^-: investigation of the role of metastable ions in a combined experimental and theoretical study". In: *Physical Chemistry Chemical Physics* 23.43 (Nov. 10, 2021). Publisher: The Royal Society of Chemistry, pp. 24607–24616. ISSN: 1463-9084. DOI: 10.1039/D1CP03977F. URL: https://pubs.rsc.org/en/content/articlelanding/2021/cp/d1cp03977f.

[21] Gustav Eklund et al. "Cryogenic merged-ion-beam experiments in DESIREE: Final-state-resolved mutual neutralization of Li^+ and D^-". In: *Physical Review*

A 102.1 (July 30, 2020). Publisher: American Physical Society, p. 012823. DOI: 10.1103/PhysRevA.102.012823. URL: https://link.aps.org/doi/10.1103/PhysRevA.102.012823.

[22] E. Bäckström et al. "Storing keV Negative Ions for an Hour: The Lifetime of the Metastable $^2P^0_{1/2}$ level in $^{32}S^-$". In: *Physical Review Letters* 114.14 (Apr. 6, 2015). Publisher: American Physical Society, p. 143003. DOI: 10.1103/PhysRevLett.114.143003. URL: https://link.aps.org/doi/10.1103/PhysRevLett.114.143003.

[23] *Source of Negative Ions by Cesium Sputtering - SNICS II*. URL: https://www.pelletron.com/wp-content/uploads/2017/02/SNICS-v2.pdf.

[24] K. O. Nielsen. "The development of magnetic ion sources for an electromagnetic isotope separator". In: *Nuclear Instruments* 1.6 (Dec. 1, 1957), pp. 289–301. ISSN: 0369-643X. DOI: 10.1016/0369-643X(57)90025-7. URL: https://www.sciencedirect.com/science/article/pii/0369643X57900257.

[25] R.H. Dalitz. "CXII. On the analysis of τ-meson data and the nature of the τ-meson". In: *The London, Edinburgh, and Dublin Philosophical Magazine and Journal of Science* 44.357 (1953), pp. 1068–1080. DOI: 10.1080/14786441008520365. eprint: https://doi.org/10.1080/14786441008520365. URL: https://doi.org/10.1080/14786441008520365.

[26] I. D. Petsalakis, G. Theodorakopoulos, and R. J. Buenker. "Radiative dissociation and predissociation in HeH and NeH: A theoretical treatment using square-integrable functions". In: *Phys. Rev. A* 38 (8 Oct. 1988), pp. 4004–4008. DOI: 10.1103/PhysRevA.38.4004. URL: https://link.aps.org/doi/10.1103/PhysRevA.38.4004.

[27] S Datz and M Larsson. "Radiative lifetimes for all vibrational levels in the $X^1\,\Sigma^+$ State of HeH^+ and its relevance to dissociative recombination experiments in ion storage rings". In: *Physica Scripta* 46.4 (Oct. 1992), p. 343. DOI: 10.1088/0031-8949/46/4/005. URL: https://dx.doi.org/10.1088/0031-8949/46/4/005.